A GCSS BOUNDARY-LAYER CLOUD MODEL INTERCOMPARISON STUDY OF THE FIRST ASTEX LAGRANGIAN EXPERIMENT

CHRISTOPHER S. BRETHERTON*
University of Washington, Seattle, Washington, U.S.A.

STEVEN K. KRUEGER
University of Utah, U.S.A.

MATTHEW C. WYANT
University of Washington, Seattle, Washington, U.S.A.

PETER BECHTOLD
Laboratoire d'Aerologie, Toulouse, France

ERIK VAN MEIJGAARD
Royal Netherlands Meteorological Institute, De Bilt, Netherlands

BJORN STEVENS
Colorado State University, Ft. Collins, Colorado, U.S.A.

JOAO TEIXEIRA
ECMWF, Reading, England

(Received in final form 15 June 1999)

Abstract. Three single-column models (all with an explicit liquid water budget and comparatively high vertical resolution) and three two-dimensional eddy-resolving models (including one with bin-resolved microphysics) are compared with observations from the first ASTEX Lagrangian experiment. This intercomparison was a part of the second GCSS boundary-layer cloud modelling workshop in August 1995.

In the air column tracked during the first ASTEX Lagrangian experiment, a shallow subtropical drizzling stratocumulus-capped marine boundary layer deepens after two days into a cumulus capped boundary layer with patchy stratocumulus. The models are forced with time varying boundary conditions at the sea-surface and the capping inversion to simulate the changing environment of the air column.

The models all predict the observed deepening and decoupling of the boundary layer quite well, with cumulus cloud evolution and thinning of the overlying stratocumulus. Thus these models all appear capable of predicting transitions between cloud and boundary-layer types with some skill. The models also produce realistic drizzle rates, but there are substantial quantitative differences in the cloud cover and liquid water path between models. The differences between the eddy-resolving model results are nearly as large as between the single column model results. The eddy resolving models give a more detailed picture of the boundary-layer evolution than the single-column models, but are still sensitive to the choice of microphysical and radiative parameterizations, sub-grid-scale turbulence models, and probably model resolution and dimensionality. One important example of the differences seen in these parameterizations is the absorption of solar radiation in a specified cloud layer, which varied by a factor of four between the model radiation parameterizations.

* Author for correspondence: Dr. Christopher S. Bretherton, University of Washington, Department of Atmospheric Sciences, Box 351640, Seattle, Washington 98195-1640. E-mail: breth@atmos.washington.edu

Boundary-Layer Meteorology **93:** 341–380, 1999.

Key words: Cloud-topped boundary layers, Stratocumulus, Drizzle, Cloud-radiation feedback, Entrainment, Large-eddy simulation.

1. Introduction

Marine cloud-topped boundary layers are a particularly important problem for numerical weather forecast models, atmospheric global circulation models (GCMs), and coupled ocean-atmosphere models because of their impact on the Earth's radiation budget (Hartmann et al., 1992) and on the tropical general circulation (Tiedtke et al., 1988). Predictions of the boundary-layer structure and cloud properties in a large-scale model are heavily reliant on physical parameterizations that must properly represent the tight feedbacks between boundary-layer convection, surface fluxes and drag, cloud microphysics and radiation, and entrainment of the overlying air. The subtropical stratocumulus regions off the west coasts of major continental land-masses have been a particularly obvious problem. Instead of maxima in low cloud cover of 60–80% in these regions (Klein and Hartmann, 1993), most GCMs and forecast models predict minima in low cloud cover of 20% or less, reflecting the mean subsidence of dry air that typifies the free troposphere in these regions (CCM3, 1997; Fowler and Randall,1996; Del Genio et al., 1996). A few models, such as recent versions of the European Centre for Medium Range Weather Forecasts (ECMWF) model (Tiedtke, 1993) have improved the climatology of low cloud cover in the subtropics by careful coupling of the cloud cover, shallow convection, vertical diffusion, and radiation parameterizations, but even these models have significant regional problems with cloud properties and radiative fluxes.

While global radiation datasets such as obtained in the Earth Radiation Budget Experiment, and global cloud cover datasets such as obtained by the International Satellite Cloud Climatology Project, can help diagnose problems, they are not so useful in understanding the model deficiencies. Regional datasets from intensive programs allow a much more detailed comparison of the models and observations. For comparing with measurements at a point or sub-grid-scale region, a 'single-column model' approach is often useful. Advective tendencies of forecast variables in an atmospheric column are measured or calculated from gridded analyses, while the nonadvective tendencies of prognostic variables in the column are predicted by the model's physical parameterizations.

A difficulty with this approach is that advective tendencies may be quite uncertain. Both horizontal and vertical advective tendencies contribute to this uncertainty. Mean vertical motion from gridded global analyses is particularly unreliable, and is also hard to deduce accurately from in-situ measurements. A secondary issue is that horizontal advective tendencies of variables such as cloud cover and liquid water content are not routinely measured and generally are not well known, even in periods of intensive field observations during regional experiments.

The Atlantic Stratocumulus Transition Experiment (ASTEX) took place in the northeastern subtropical Atlantic Ocean in June 1992 (Albrecht et al., 1995). Its goal was to study the processes responsible for cloudiness transitions between stratocumulus and subtropical trade cumulus cloud. During ASTEX, two 'Lagrangian' experiments were carried out, in which a column of boundary-layer air was almost continuously sampled for 36–42 hours by aircraft as it drifted with the mean boundary-layer wind. Bretherton and Pincus (1995, hereafter BP95) and Bretherton et al. (1995, hereafter BAS95) describe some overall results of these experiments. These Lagrangian experiments provide exciting tests for physical parameterization schemes, because they provide a comprehensive suite of measurements in which the uncertainties associated with horizontal advection are largely eliminated. For similar reasons, the ASTEX Lagrangian experiments are equally attractive for comparison with eddy-resolving numerical models, in which the circulations within a column of boundary-layer air of O(10 km) on a side are modelled at high resolution. To compare such models to a Lagrangian dataset, the variations of the free-tropospheric conditions, mean vertical velocity profile, downwelling radiation, the sea-surface temperature and the geostrophic winds are treated as time-varying boundary conditions to the model (Krueger et al., 1995; Wyant et al., 1997).

In this paper we describe an intercomparison study in which three eddy-resolving models and three single-column models were used to simulate the first ASTEX Lagrangian experiment of June 12–14, 1992, which we will henceforth call Lagrangian 1 or L1. This was one of an annual series of intercomparisons organized by the Boundary Layer Cloud working group of GCSS (the Global Energy and Water Experiment Cloud System Study (GCSS Cloud System Science Team, 1993)), and preliminary results were discussed at a workshop in De Bilt, Netherlands, in August 1995.

A goal of GCSS is to use highly spatially resolved numerical models of cloud systems to improve parameterizations used in large-scale models. Some studies have used idealized cases to focus on individual physical processes. In the current study, the marine boundary-layer (MBL) structure was complex; the diurnal cycle, drizzle processes, stratocumulus cloud and cumulus convection all played roles. The MBL evolution was modelled for the full observational period of almost two days, much longer than the 1–6 hours that has been typical for three-dimensional eddy-resolving model studies. For both of these reasons, we anticipated that details of the radiation, microphysical and surface-flux parameterizations all might substantially affect the overall boundary-layer evolution, leading to large, and hopefully illuminating, disagreements between the eddy-resolving models, the single- column models and the observations.

The length of the simulation limited our intercomparison to two-dimensional (2D) eddy-resolving models. A shorter intercomparison study of three-dimensional (3D) eddy-resolving models based on days 13.25 to 13.5 of L1 was started by the GCSS boundary-layer working group in 1995 and was the subject of a further workshop in August 1996. Several recent studies (Moeng et al., 1995; Bretherton

et al., 1999) have shown that there are significant differences between the turbulence statistics and entrainment rates in 2D vs. 3D boundary layers. These can be expected to have some impact on the 2D simulations presented, but our collective modeling experience suggested that the 2D results should nevertheless be a useful guide to problems we would also likely encounter in 3D simulations, and therefore it would be useful to document their performance for this complex MBL. Three-dimensional eddy-resolving model simulations of 1–2 days simulated time are now becoming computationally feasible; we hope this intercomparison serves as inspiration for 3D simulations of L1.

In Section 2 we briefly describe L1 and how the observations were converted to a form convenient for forcing eddy resolving and single column models. In Section 3 we describe salient features of the participating models. In Section 4 we describe the results of the intercomparison, including boundary-layer vertical structure, cloud fractional cover, liquid water content, precipitation, radiation, surface fluxes and turbulence. Section 5 discusses a sensitivity study, and Section 6 briefly discusses a second GCSS intercomparison of ASTEX Lagrangian 2. Section 7 presents conclusions.

2. The Lagrangian 1 Observational Dataset

L1, schematically illustrated in Figure 1, took place in a clean marine air mass with moderate to high (10 m s^{-1}) wind speeds and cloud droplet concentrations of 100 cm^{-3}. During the 42-hour period when the boundary-layer air column was tracked (1600 UTC 12 June–1000 UTC 14 June, 1992), it advected 1400 km southward then southwestward from (41°N, 24°W) to (29°N, 29°W), skirting east of the Azores Islands. Over this distance, the sea-surface temperature (SST) increased over 4 K from 290 to 294 K, with a particularly rapid rise as the air parcel advected over the Azores Current between 0000 and 1200 UTC on June 13. In the first day of L1, the MBL was 70–100 hPa deep, capped by a solidly overcast, drizzling stratocumulus layer. During the next day the MBL rapidly deepened to a 160-hPa thick layer with cumuli rising into broken stratocumulus and some deeper cumulus congestus penetrating the trade inversion. The L1 case study tests our ability to model two important and imperfectly understood MBL processes, drizzle formation and stratocumulus cloud breakup.

Aircraft measured winds averaged over the boundary-layer depth were used to determine the air column trajectory. Unfortunately, low cloud ceilings at the aircraft operations centre forced a 14 hour gap in aircraft data coverage starting near 0000 UTC 14 June, during which the actual air parcel trajectory and boundary-layer evolution is somewhat conjectural. During the remainder of L1, 17 aircraft soundings through the MBL were taken along the trajectory, from which BP95 derived a time-height cross-section of the MBL evolution. Horizontal legs at several heights within and above the MBL provided measurements of SST, cloud cover, drop size

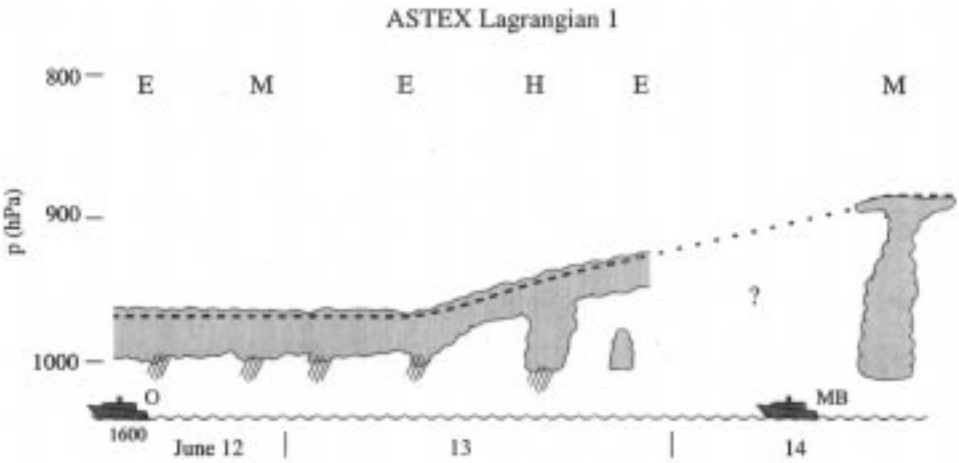

Figure 1. Lagrangian boundary-layer evolution during L1. Letters at top indicate times of aircraft flights of the NCAR Electra (E), UKMRF C130 (M), and UW C131a (H). Ships were also stationed at beginning and end of trajectory, as shown at bottom.

distribution and drizzle, radiative fluxes (see below) and turbulence. This wealth of data, summarized in Table I, provides both the initial and boundary conditions ('forcings') and the verification for single-column and eddy-resolving models. We will discuss the verification data further in Section 3. In the remainder of this section, we discuss the specification of forcings for the models.

2.1. FORCINGS

For numerical simulations, it is convenient to specify the forcings at regular time intervals. For this study, the forcing fields were all interpolated to hourly values, and linear time interpolation was used to specify the forcings at other times. For this study, only the boundary-layer evolution is predicted by the models; conditions are relaxed to the observed values above the predicted boundary-layer top, as discussed in Section 3.4. In addition to initial thermodynamic and wind soundings, the following boundary conditions were specified during the simulated time period:

1. SST.
2. Mean vertical velocity at all levels in and above the MBL.
3. Mean winds at all levels in and above the MBL.
4. Temperature and mixing ratio above the boundary layer.
5. Downwelling radiative fluxes at 700 hPa, a level above the boundary-layer top, for models that did not calculate radiative fluxes over the entire atmospheric column.
6. Droplet concentration (used by some models).

TABLE I

Observational datasets for Lagrangian 1. Leg averages are taken over 60 km horizontal flight legs stacked at representative heights within the boundary layer. The NCAR Electra, UKMRF C130, and University of Washington C131a were the three participating research aircraft during L1. 'Lowest leg' aircraft observations were taken at 30 m during daylight and 150 m at night. M95, D95, RD96, RD97 and AB97 refer to Martin et al. (1995), Duynkerke et al. (1995), de Roode and Duynkerke (1996, 1997) and Austin and Bretherton (1997). MAGE refers to papers in a special issue of *J. Geophys. Res.* **101**, 4317–4514. PRT radiometers detect a narrow range of wavelengths in the water vapour window. The FSSP is a cloud droplet probe.

Field	Type	Source	Reference
u, v, T, q_v, q_l, N	Soundings	Electra, C130, C131a	BP95 (see also RD97)
SST	Surface	Ship, ECMWF	BAS95
	Lowest legs	Electra, C130 PRT	BAS95
Near surface T, q_v	Lowest legs	Electra	BAS95
Cloud fraction	Leg avg.	Electra, C130 FSSP	BAS95, RD97
	Leg avg.	Upward PRT	BAS95
	Area avg.	METEOSAT	BAS95, M95
Drizzle rate, freq.	Leg avg.	Electra, C130 probes	BAS95, RD97
Droplet spectra	Leg avg.	C130 hour 8–23	D95, RD96
In-cloud N	Leg avg.	Electra, C130 FSSP	BAS95
Radiative fluxes	Leg avg., snd.	C130 hour 8–23	D95, RD96
	Leg avg., snd.	C130, Electra	AB97
$\overline{w'q_t'}$, $\overline{w'T'}$	Leg avg.,	C130, Electra	RD97 (see also D95, RD96)
Velocity variances	Leg avg.	C130, Electra	RD97 (see also D95, RD96)
Aerosols, chemistry	Various	Aircraft, ship	MAGE

2.2. VERTICAL MOTION AND SST

In L1, the horizontal wind vector varied only slightly with height within and even above the boundary layer, so mean horizontal advection of temperature and mixing ratio relative to the Lagrangian frame were neglected. The mean vertical motion at the height of the boundary-layer top was deduced by BAS95 using a combination of several methods (ECMWF operational analyses, a water budget of the MBL, ozone fluxes and jumps, and the apparent vertical motion of isosurfaces of water and ozone in the air column above the MBL), all of which had O(50%) uncertainties and poor temporal resolution. Within these uncertainties, all four estimates of the mean vertical motion were consistent, and were combined into a 'best guess' estimate. For forcing the models, we assumed that the vertical motion increased linearly with height through the boundary layer, which is equivalent to assuming a constant horizontal divergence of the mean winds. The implied 'best-guess' divergence within the MBL is shown in Figure 2. Above the top of the MBL, a height-

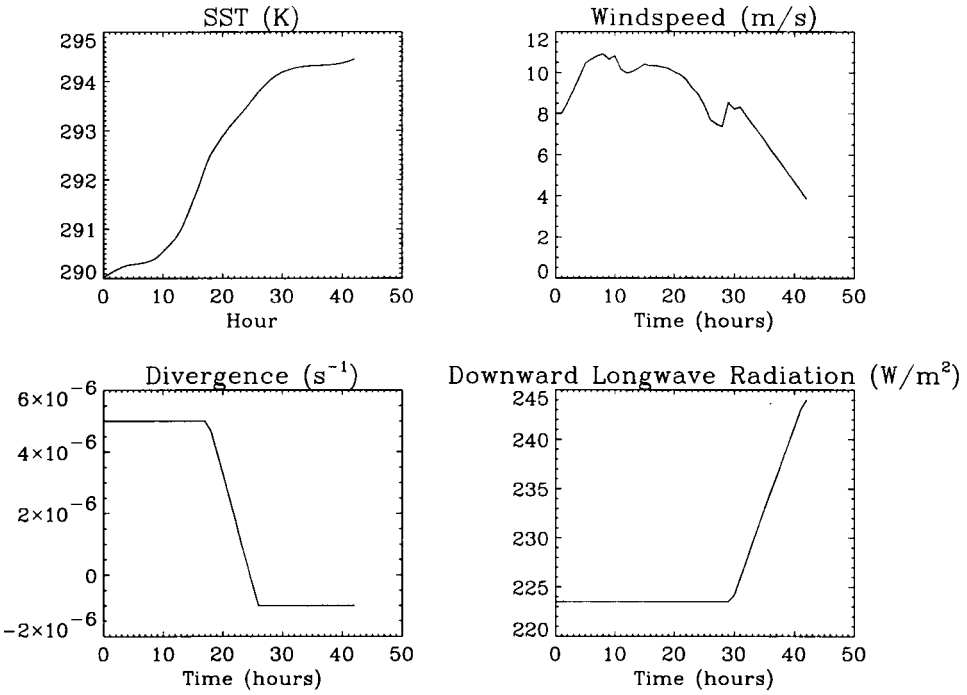

Figure 2. 'Best-guess' observed horizontal divergence and SST following the air column trajectory during L1.

independent subsidence rate was applied; since the above-MBL thermodynamic profiles were relaxed to observed profiles (see below), the assumed subsidence above the MBL has almost no impact on the simulations. The 'best guess' SST of BAS95, derived from a combination of ship and aircraft measurements, is also shown in Figure 2.

2.3. SPECIFICATION OF WINDS

Ideally, the vertical profile of geostrophic wind should be specified and the simulated wind field should evolve accordingly; this requires observations of the geostrophic wind. Geostrophic winds were not accurately measured by the aircraft, and along the trajectory of L1 were deduced from routine ECMWF analyses. These six-hourly analyses were interpolated from the 31 ECMWF model levels to 25-hPa vertical resolution, with 1.125 degree horizontal resolution. The geostrophic wind was calculated at the nearest gridpoint to the instantaneous trajectory position every hour, using centered space differencing and linear time interpolation of the geopotential height field. However, we found that the computed geostrophic winds were not in good agreement with the observed winds, even above the boundary layer. To avoid introducing large errors in the model evolution due to wind-induced errors

in the surface fluxes, we chose to relax the horizontally averaged wind profiles to their observed values with a three-hour relaxation timescale.

2.4. TEMPERATURE, MOISTURE AND WIND PROFILES

In BP95, time-height sections based on the 17 soundings taken during L1 were presented. These soundings were unsmoothed except for vertical averaging into 2 hPa intervals. For comparison with models, it was useful to smooth over some of the short-period sampling variability evident in those sections. Using an algorithm described in the Appendix, we produced smoothed hourly soundings that preserved the sharpness of the inversion seen in individual soundings and blended those with ECMWF analyses above the top of the aircraft soundings for radiative transfer calculations. Smoothed hourly soundings of the thermodynamical fields and winds are shown in Figure 3. The MBL was capped by a 2–4 K inversion throughout L1. Initially, there was no decrease of mixing ratio above the inversion, but by the end of L1, the MBL was twice as moist as the overlying air. Early in L1, horizontally averaged cloud liquid water contents were typical of stratocumulus. Stratocumulus liquid water content decreased considerably and the overlying stratocumulus became patchy during the last 12 hours as MBL cumulus convection became vigorous. The soundings show that variations of wind with height were fairly small, although there was some wind shear across the inversion. They also show the wind turning from northerly to north-easterly at all heights after hour 17. We note that the hourly soundings in the middle of the 'data gap' from hours 28–42 are based purely on interpolation, and are less reliable than at other times.

2.5. DOWNWELLING RADIATIVE FLUXES

Infrared satellite imagery (BP95) indicated that there was almost no cloud above the boundary layer in the L1 air column until day 14.3. Thus, the downwelling radiative fluxes above the boundary layer could be estimated by a clear air radiative transfer model. Austin and Bretherton (1997) analyzed broadband radiative fluxes from aircraft during ASTEX. They found good agreement between the downwelling longwave radiation measured on the UKMRF C130 aircraft during L1 and that deduced from the hourly soundings using the four-stream code of Fu and Liou, which was described by Krueger et al. (1995). Their calculations assumed the standard midlatitude summertime sounding of McClatchey (1972) above 100 hPa.

2.6. DROPLET CONCENTRATION

The microphysical and radiation parameterizations in some of the models in the intercomparison depended on cloud droplet concentration or mean droplet size. We chose a droplet concentration $N = 100$ cm^{-3} at all heights and times based on

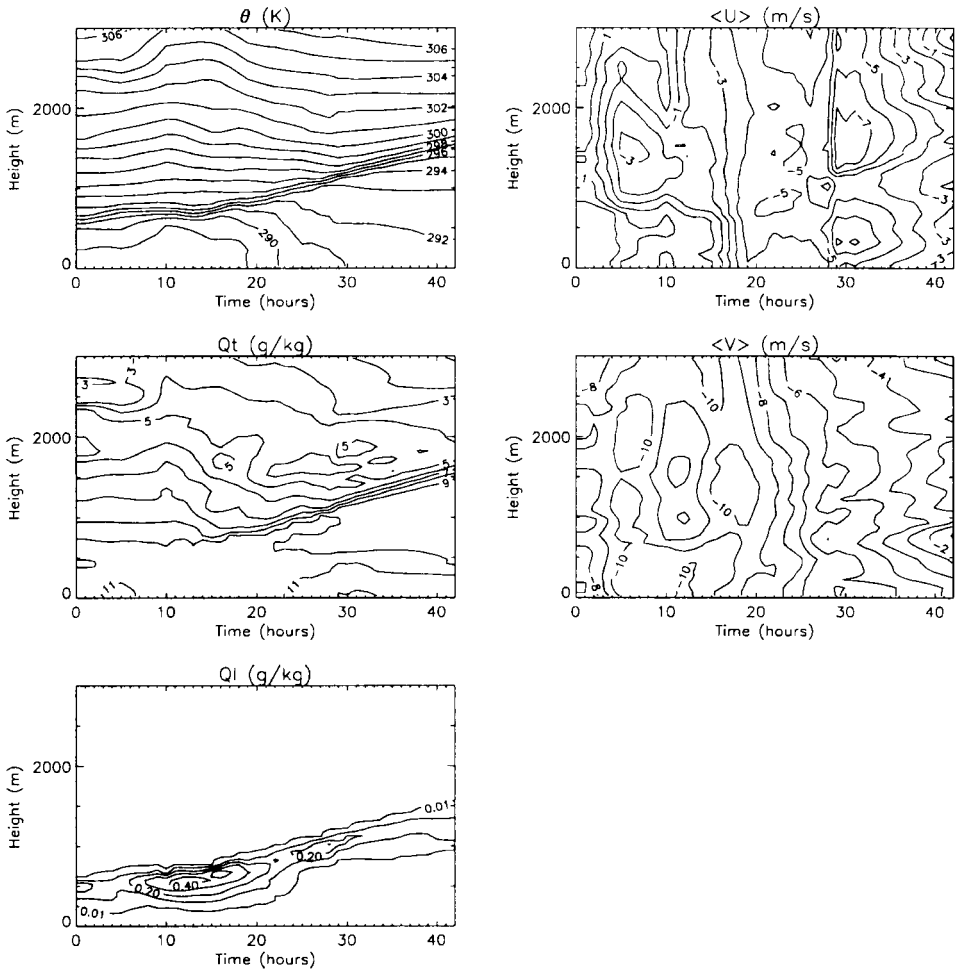

Figure 3. Smoothed hourly horizontally-averaged fields following the L1 trajectory, based on aircraft soundings of BP95 extrapolated upward using ECMWF analyses: (a) θ (contour interval 1 K), (b) Total water mixing ratio q_t (contour interval 0.5 g kg^{-1}), (c) Liquid water content q_l (contours at 0.01 g kg^{-1}, then at multiples of 0.1 g kg^{-1}), (d) Eastward wind component u (contour interval 1 m s^{-1}), (e) Northward wind component v (contour interval 1 m s^{-1}).

the FSSP measurements from in-cloud segments of level flight legs of L1 (shown in Figure 5 of BAS95.)

TABLE II
Models intercompared.

Acronym	Scientist	Type	Vertical gridspacing	Reference
ECMWF	J. Teixeira	1D	25–45 hPa	Tiedtke (1993)
AERO	P. Bechtold	1D	50 m	Bechtold et al. (1992)
KNMI	E. v. Meijgaard	1D	10 hPa	See Section 3
CSU	B. Stevens	2D	50 m	Stevens et al. (1996)
UU	S. Krueger	2D	50 m	Krueger et al. (1995)
UW	M. Wyant	2D	50 m	Wyant et al. (1997)

3. Setup of the L1 Case Study

3.1. Description of the models

This study compares results from three eddy-resolving and three single column models, listed in Table II. All of the models were developed largely independently. The KNMI single-column model blended the microphysical and convection parameterizations of the ECHAM3 atmospheric general circulation model (Roeckner et al., 1992) with the radiation scheme of the ECHAM4 model (Roeckner et al., 1996), and the non-local vertical diffusion scheme of Holtslag and Boville (1993) for dry boundary-layer mixing. The ECMWF column model was a single-column version of Cycle 13R4 of the ECMWF operational forecast model. The AERO model has been extensively compared against observations of a variety of boundary-layer cloud types. Its most notable difference from the other two 1D schemes was its use of a turbulence closure model for all dry and moist mixing, with no cumulus parameterization. Moeng et al. (1996) include a discussion of the finite-differencing algorithms, sub-grid-scale turbulence schemes, condensation and longwave radiation schemes in the eddy-resolving models. In the L1 intercomparison, precipitation formation, shortwave radiation, and surface fluxes were also important. Some salient characteristics of the individual models are discussed in more detail below.

3.1.1. *Cloud Formation and Microphysics*

The CSU model used a bin-resolved calculation of the droplet spectrum to calculate the formation of drizzle. The UU and UW models used Kessler-type bulk microphysical schemes. The UW model assumed instantaneous and uniform cloud formation within a grid box if the grid point at its centre is saturated. The UU model calculated the fraction of saturated air in a grid box based on moments of the conserved variables θ_l and q_t derived from its third-order sub-grid-scale turbulence

closure. This closure also provided sub-grid-scale fluxes of θ_l, q_t, buoyancy, and liquid water.

The 1D models all incorporated some parameterization of fractional cloudiness/condensation within a grid level. The AERO model used a 1.5-order turbulence closure scheme to deduce the θ_i and q_t fluxes and second-order moments. An assumed joint probability distribution for q_t and w based on these moments determined the fraction of air that is saturated, and the liquid water and buoyancy fluxes at each level. The ECMWF model prognosed how fractional cloud cover and liquid water content evolve at each grid level in response to a number of physical processes, such as detrainment from moist convection, lateral mixing, cloud-top radiative cooling and large-scale vertical motion (Tiedtke, 1993).

The KNMI model treated only liquid water content as a prognostic variable. Layer cloud fraction was calculated with a cloud scheme proposed by Sundqvist (1978). Sources and sinks of heat and water vapour were partitioned uniformly over the cloudy and clear parts of the grid-box. Cloud fraction was diagnosed on the basis of a threshold relative humidity. In both the ECMWF model and in the KNMI model the conversion of cloud water into precipitation was parameterized with a scheme proposed by Sundqvist et al. (1989). In the KNMI model the contribution from coalescence was also taken into account following a formulation by Smith (1990).

3.1.2. *Radiative Transfer*

The radiative transfer schemes used in the models varied widely in complexity. All models used two-stream radiative transfer codes, except the UU model, which used a four-stream code. All of the 2D models used the independent pixel approximation, in which radiative transfer through each grid column is treated independently of other grid columns using the assumption of a plane-parallel cloud. The radiation codes used in the three 2D models were all independently developed.

The ECMWF, AERO and KNMI 1D models used variations of Morcrette's (1991) scheme. In the KNMI model, the ECHAM4 version of this scheme (Roeckner et al., 1996) was used, in which the treatment of cloud optical properties, the water vapour continuum, and trace gases are modified. The 1D models all assumed maximum-random overlap (maximum overlap of vertically contiguous clouds, and random overlap of vertically separated cloud) to deduce radiative fluxes from the model-predicted cloud fraction and cloud liquid water at each level within the boundary layer.

3.1.3. *Surface Fluxes*

All models had similar bulk aerodynamic schemes for predicting surface fluxes. The schemes were all based on Monin–Obuhkov similarity theory with a wind-speed dependent roughness length, except the UW scheme, which used a wind-speed dependent transfer coefficient appropriate for neutral stability. The formu-

lation of the roughness length and the universal functions used in the similarity theory differed somewhat between models.

3.2. Spatial resolution, domain size, and simulation length

The domain size used for all eddy-resolving models was 3 km high by 6.4 km wide, with vertical grid spacing Δz = 50 m and horizontal grid spacing Δx = 100 m. Periodic boundary conditions were imposed in the horizontal. For the single column models the same vertical resolution was used except as noted in Table II. All models were run for 42 hours from day 12.67 to day 14.42.

3.3. Initialization

The models were initialized using the hourly wind and temperature sounding at 1600 UTC on June 12, 1992 (Day 12.67) at the beginning of L1. For eddy resolving models, a horizontally uniform initial sounding was used, and convection was triggered by adding spatially uncorrelated random perturbations uniformly distributed between -0.1 and 0.1 K to the initial temperature field at all gridpoints below the initial inversion height. The most obvious choice for initial soundings of q_v and θ was the first hourly-smoothed sounding derived from the observations. Due to measurement inaccuracies, horizontal inhomogeneity, the averaging procedure, and approximations in the formulae for saturation mixing ratio used in the models, the water vapour mixing ratio in this sounding need not be saturated, even though mean liquid water was found to be present. Because of the strong feedbacks between clouds and radiation, we decided to initialize all models with the same profile of liquid water. Hence, at pressure levels at which sufficient cloud was present we initialized each model with the model-derived saturation water vapour mixing ratio at the sounding pressure and temperature at that level, instead of using the water vapour mixing ratio from the first hourly sounding. Sufficient cloud was assumed to be present at levels at which either (i) the horizontally averaged droplet concentration at that level is at least 0.5 as large as the estimated in-cloud droplet concentration or (ii) the liquid water mixing ratio q_l is at least 0.05 g kg^{-1}. At cloudy levels, q_l was initialized to the observed value.

3.4. Other details

In addition to the velocity relaxation described in Section 2, the thermodynamic fields in all models except ECMWF were relaxed toward the time-dependent observed profiles with a three-hour time constant at all levels at least 150 m above a nominal inversion height, similar to a procedure used by Wyant et al. (1997). The goal of this procedure was to impose realistic above-inversion conditions while minimally affecting the entrainment dynamics within the inversion layer of the models. The 150-m buffer depth of no relaxation was designed to allow the models to determine how penetrative convective updrafts and their radiative feedbacks

may modify the thermodynamic structure within the inversion zone, rather than imposing this from observations.

The appropriate choice of the nominal inversion height is subtle, and different participants inadvertently used somewhat different specifications. Initially, we specified the nominal inversion height to be the model-derived inversion height. This is fine when the model inversion is at least as deep as the observed inversion, but if the model inversion is significantly shallower, some grid levels above the model inversion may be relaxed to observed conditions below the inversion. This will rapidly raise the model inversion to become comparable to the observed inversion. The nominal inversion height ultimately specified for the intercomparison was the observed inversion height. This is a better choice unless the model inversion is significantly deeper than was observed, in which case the relaxation may relax some grid levels below, or within the model inversion, to conditions above the observed inversion. This will rapidly lower the model inversion to become comparable to the observed inversion. The results shown for all models, except UW and ECMWF, used this procedure (though the KNMI model relaxed at all levels above the nominal inversion, rather than adding the 150-m buffer zone). The UW model tended to produce an excessively deep inversion. Rather than suppress this tendency, it was decided to use the model inversion height as the nominal inversion height for relaxation. In the ECMWF model, the sounding was specified above 700 hPa, and no relaxation was done below this level. In retrospect, specifying the nominal inversion height to be the maximum of the model-derived and observed inversion heights would have worked well for all models, but this was not done.

All models incorporated a diurnal cycle of insolation appropriate to the date and the (changing) latitude and longitude. The sea-surface albedo for shortwave radiation was set to 0.05, and the solar constant was set to 1323 W m^{-2}, a value appropriate for the earth-sun distance in mid-June.

The Coriolis force was included in most models, based on the instantaneous trajectory latitude. However, the velocity relaxation made the physically based acceleration terms in the momentum equations largely irrelevant.

4. Results

4.1. VERTICAL PROFILES

Overall, both the 2D and the 1D models simulated the MBL evolution well. Figure 4 shows the time evolution of the inversion height z_i, identified as the horizontal average over all columns of the centre of the grid layer across which there was the strongest decrease in q_t with height. All simulations were in remarkably good agreement with the observations except for the UW model, which over-deepened the inversion after hour 25. This may be related to the overestimation of cloud fraction in this model (see below), which resulted in strong cloud-top longwave cooling

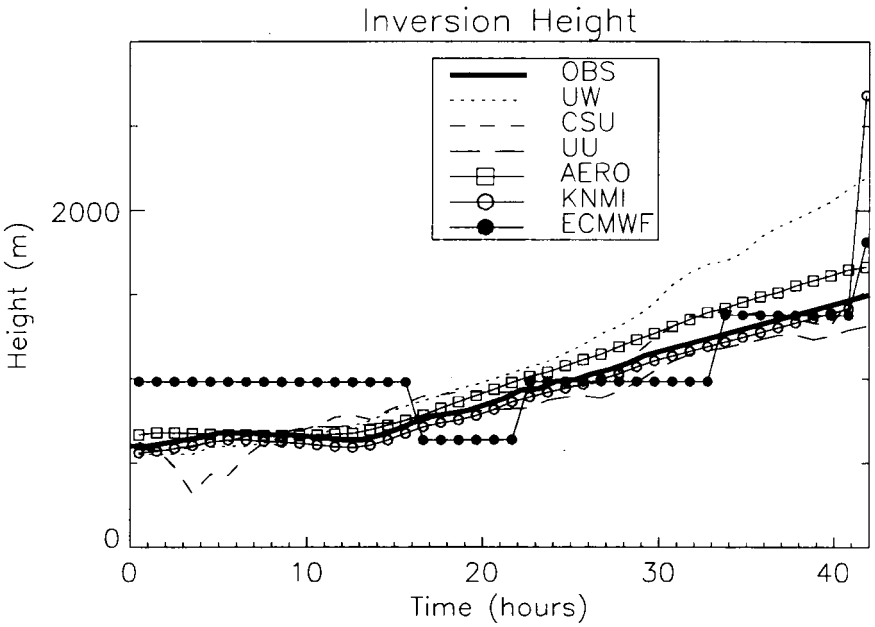

Figure 4. Observed and modelled evolution of inversion height during L1.

and more entrainment. However, comparison of the energy budget of this and the other 2D models did not show differences as large as would be needed to explain the nearly 100% higher entrainment rate than the other models or observations.

Figure 5 shows soundings of θ and q_v at hour 15. The agreement between models above the inversion was forced by the relaxation of θ and q_v toward the hourly interpolated observed profile. However, even the ECMWF model, in which relaxation was not used, was very close to the observed above-inversion profile. Since the vertical wind shear is small at all heights, it is a fair approximation to assume that the Lagrangian column also includes the air above the boundary layer. In this case, a Lagrangian column model with no horizontal advective forcing should be able to predict the above-boundary-layer evolution as well as the MBL evolution. The agreement of all models with the observed soundings in and below the inversion was also good. All the models maintained a sharp inversion of approximately the observed height and strength. The vertical gradients of θ and q_v within the boundary layer varied somewhat between models, but were generally similar to those observed. Except in AERO, the boundary-layer profiles differed somewhat from those expected in a cloud-topped mixed layer. In particular, θ and q_v were not uniform below cloud base, presumably due to evaporating drizzle, which tends to restratify the boundary layer even as convection mixes it (Stevens et al., 1998).

Figure 6 shows soundings of θ and q_v at hour 39. The CSU and UU 2D models and the KNMI 1D model soundings of θ were very similar to the observations,

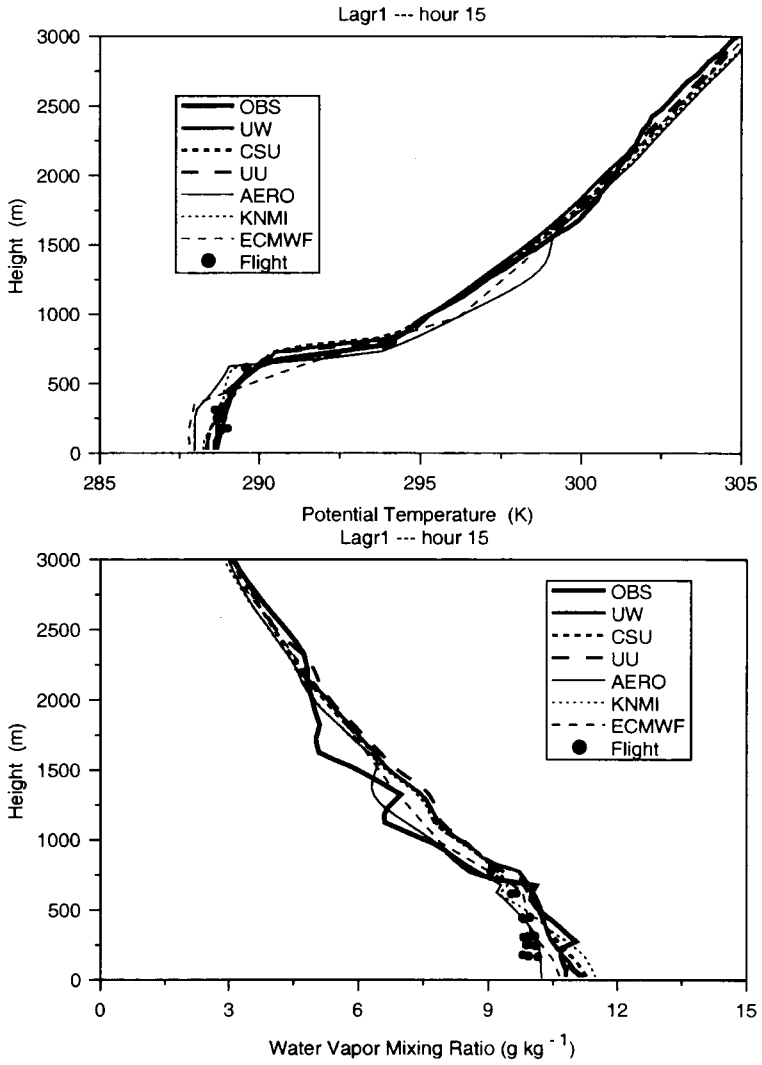

Figure 5. Horizontally averaged θ and q_v for the six models at hour 15, superposed on the hourly interpolated observed sounding (OBS) and 30 km leg averages from UKMRF flight A209 taken between hours 9 and 12.

with a well-mixed layer up to about 300–500 m above the surface, a conditionally unstable layer supporting cumulus convection, and a 7 K inversion. The UW model sounding was similar to these, but by hour 39 the inversion was almost 500 m too high. The CSU model predicted a 50% stronger stratification (3 K km^{-1}) in the cumulus layer than was observed, but the other models correctly predicted the stratification in this layer. The AERO model produced too cool and dry a sounding late in L1, resulting in an excessively deep dry-adiabatic subcloud layer and only a

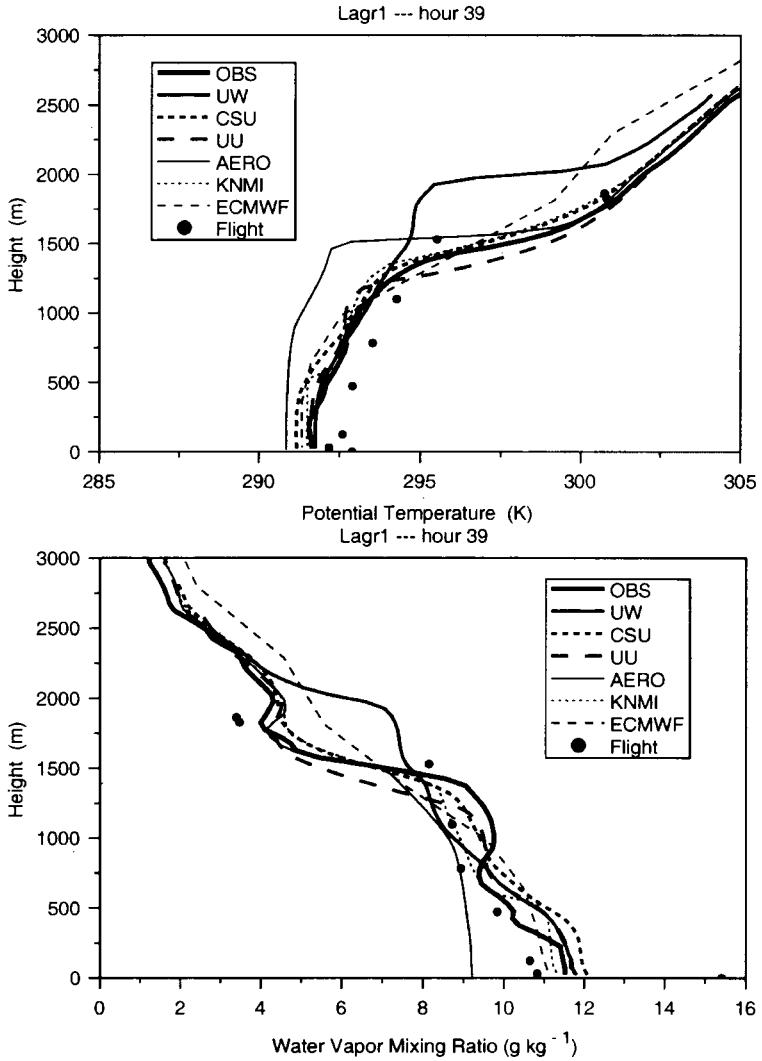

Figure 6. Horizontally averaged θ and q_v for the six models at hour 39, superposed on the hourly interpolated observed sounding (OBS) and 30 km leg averages from UKMRF flight A210 at the end of L1.

shallow layer of conditional instability. The observed moisture sounding, and those of all the models, show that the MBL was far from well mixed at hour 39. Instead, most models produced a subcloud layer about 2 g kg^{-1} moister than the cumulus layer, with a further slight decrease of moisture with height within the conditionally unstable layer. This type of 'cumulus-coupled' sounding was ubiquitous during ASTEX. It is quite encouraging that a diversity of models was able to reproduce accurately the transition from a shallow, fairly well-mixed MBL to a deep cumulus-coupled MBL.

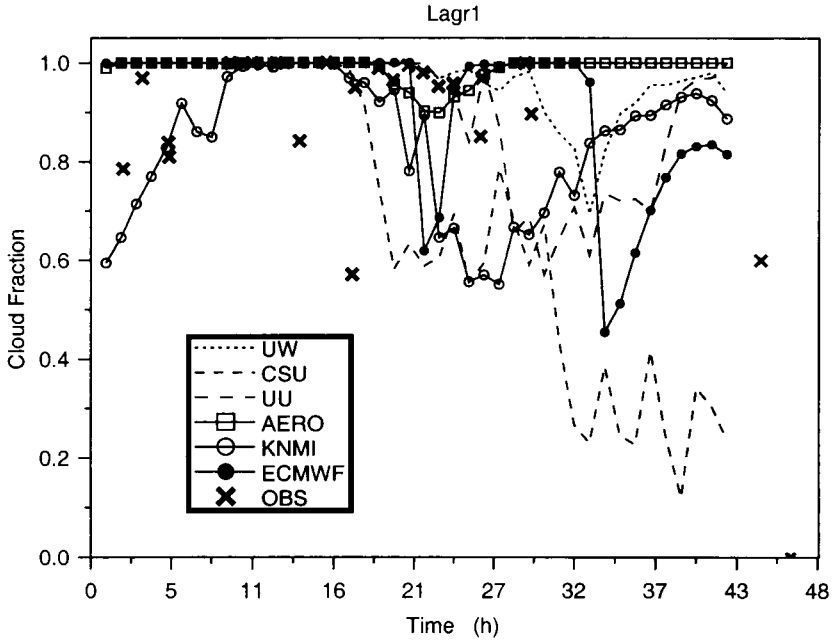

Figure 7. Cloud fraction for the six models and BAS95 observations.

Figure 7 shows the model and observed cloud fractions. For 2D models, the cloud fraction is defined as the fraction of columns with at least one gridpoint in which q_l exceeds 0.01 g kg^{-1}. Observations of cloud fraction are taken from BAS95, and derive from three sources, aircraft liquid water probes when the aircraft was flying within the cloud layer, upward pointing radiometer measurements when the aircraft was flying well below cloud base, and satellite retrievals based on excedance of a threshold cloud optical depth inferred from satellite imagery. Note that during hours 28–42, no in-situ observations were available since the aircraft were not flying, and no satellite retrievals were made because it was night, or the solar zenith angle was very large. Figures 8 and 9 show vertical profiles of the liquid water content and cloud cover predicted by the six models, averaged horizontally and over one-hour time intervals. All models produced maximum liquid water contents of around 0.4 g kg^{-1} in hours 5–17, and almost 100% cloud cover through hour 20, as observed.

Later in the simulation, as the boundary layer deepened, all models reproduced the observed evolution of cloud structure into a layer of cumulus rising into overlying stratocumulus. The signature of cumulus clouds was particularly evident in the 2D simulations, which showed small amounts of cloud and liquid water contents between 500 m and the base of the stratocumulus layer. Within the 2D models, the cloud fraction predicted in the last ten hours ranged widely from 20–30% (CSU) to nearly 100% (UW), while the corresponding liquid water content varied from less than 0.1 g kg^{-1} to over 0.2 g kg^{-1}. Overall, the UU simulation was most consistent

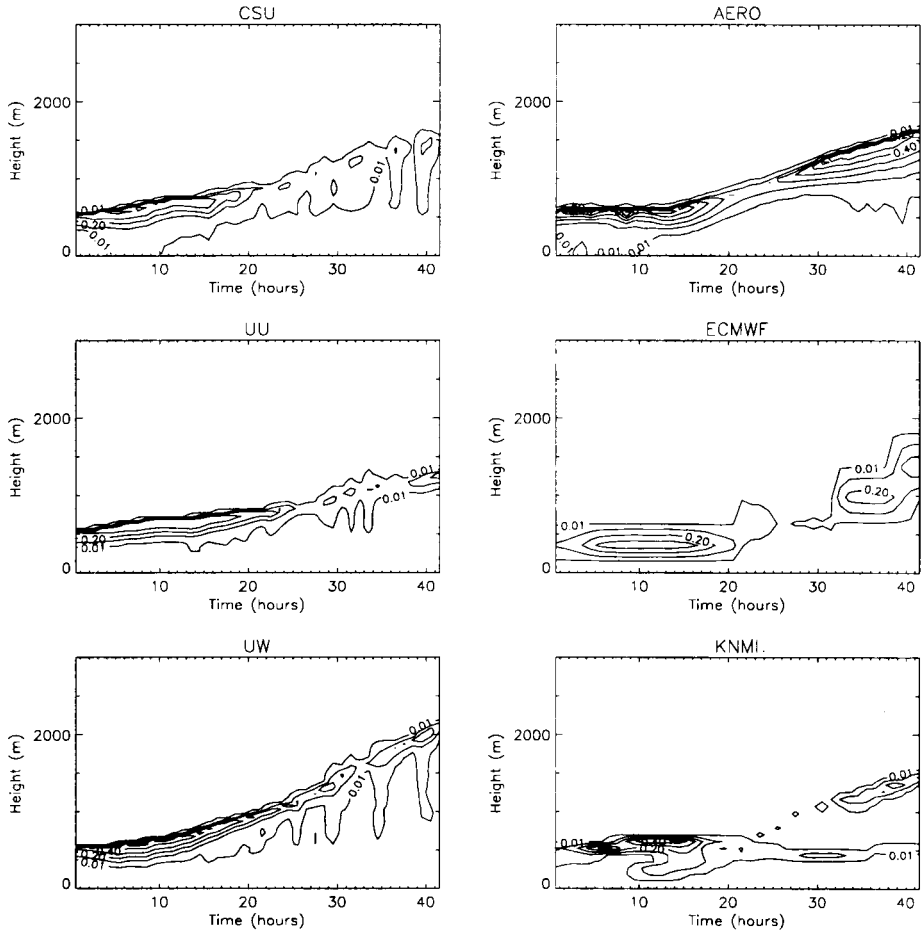

Figure 8. Horizontally averaged q_l for the six models (contours at 0.01 g kg^{-1}, then at multiples of 0.1 g kg^{-1}).

with the observations. We were not able to pinpoint reasons for the differences between the 2D simulations, because they involve many physical processes that are represented differently between the models.

Some representation of cumulus-coupling was seen even in the cloud statistics from the 1D models. In the AERO simulation, there was a zone of low liquid water contents and cloud fraction at 33–40 hours at 500–1000 m heights. In the KNMI simulation, there were multiple cloud layers after 23 hours. In this model, there was excessive cloud formed at the cumulus cloud base at 500 m, with up to 50% cloud fraction at that level. At the same time, the stratocumulus cloud fraction and liquid water content were underpredicted in hours 20–30. In the ECMWF simulation, contributions of individual physical parameterizations to the overall boundary-layer evolution were examined, and illustrate the complex interplay of

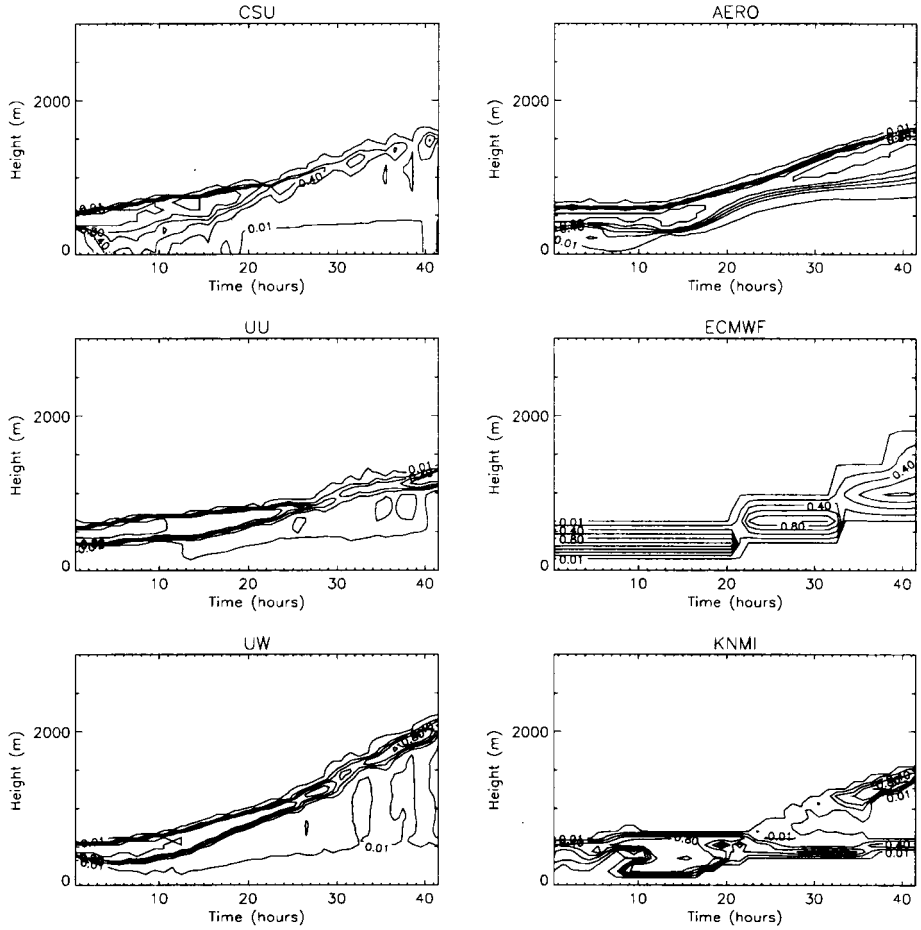

Figure 9. Horizontally averaged cloud fraction for the six models (contours at 0.01, then at multiples of 0.2).

parameterizations involved in many single column model simulations of boundary-layer cloud. The ECMWF model retained a stratocumulus cloud layer of nearly 100% cloud cover through hour 30. For the first 20 hours, the liquid water contents in this layer were realistic. Around hour 20, the cloud top moved up a grid point associated with brief activation of the convection scheme. For the next ten hours, there was no further shallow convection, and the liquid water contents in the stratocumulus layer fell to unrealistically low values of 0.01 g kg^{-1} or less. This was due to imperfect feedbacks between ECMWF's dry convection scheme, their stratocumulus scheme, which operates so long as there is a conditionally unstable layer above cloud base that is one grid level thick, and their cumulus scheme, which is activated once the conditionally unstable part of the boundary layer is at least two grid levels thick. The cumulus parameterization was reactivated at hour 32. After

this point, the MBL was cumulus-coupled. Detrainment from cumuli rapidly raised the liquid water content in the upper boundary layer to values that are even a little larger than observed. The scatter of q_l and cloud fraction between the 1D models was somewhat larger than between the 2D models, but qualitatively, the three 1D models represented the effect of decoupling on the boundary layer remarkably well.

All models except CSU showed a maximum in liquid water content and cloud thickness at hours 8–18 and a decrease in liquid water content and cloud thickness during hours 20–30, in general agreement with the observations. This is most clearly seen by comparing the vertically integrated liquid water path in the models and the hourly interpolated observations (Figure 10). The liquid water path in all models seemed to lead the observations by three hours. Two 1D models (AERO and ECMWF) greatly overestimated the liquid water path over the last 10 hours in the cumulus regime. Spikes in liquid water path in the CSU model at the end of the simulation are associated with intermittent cumulus convection. Surprisingly, the UW simulation had reasonable liquid water path despite overestimating cloud fraction; this model tends to produce overly persistent but thin stratocumulus layers beneath the trade inversion. Some of the variation seen in liquid water and cloud fraction was probably associated with the diurnal cycle of solar absorption in the clouds, but this cannot easily be isolated in a simulation in which the other boundary forcings are also rapidly changing.

One real surprise, seen in Figure 11, was the success of most of the models at reproducing the observed drizzle rate, despite a diverse range of microphysical parameterizations. Since drizzle was observed to be spatially intermittent throughout L1, one would not expect models to match individual observations of leg-averaged drizzle rate (such as the 2.7 mm day^{-1} at hour 17), but they should reproduce the typical observed rates. All models had a peak drizzle rate of at least 1 mm day^{-1} at some time between hours 5 and 17. Except for the ECMWF model, all models predicted a decrease in drizzle rates around hour 20, as suggested by the observations, though this may be exaggerated in several of the models. The 2D model with bin-resolved microphysics (CSU) predicted almost no precipitation reaching the surface after hour 20, when cumulus clouds start forming, while the 2D models with parameterized microphysics (UU, UW) predicted small to moderate amounts of intermittent precipitation falling from the cumuli. This difference may be due to more rapid autoconversion of cloud droplets to precipitation-size particles in cumulus updrafts than in the bin-resolved model. In-situ observations frequently showed more precipitation falling front detrained stratiform cloud around the cumuli than from the cumulus updrafts themselves (Martin et al., 1995). This tends to support the slower coalescence timescale of the bin-resolved model.

4.2. RADIATIVE FLUXES

One of the main motivations for a careful treatment of boundary-layer cloud in global models is the effect of such clouds on Earth's radiation budget. Radiative

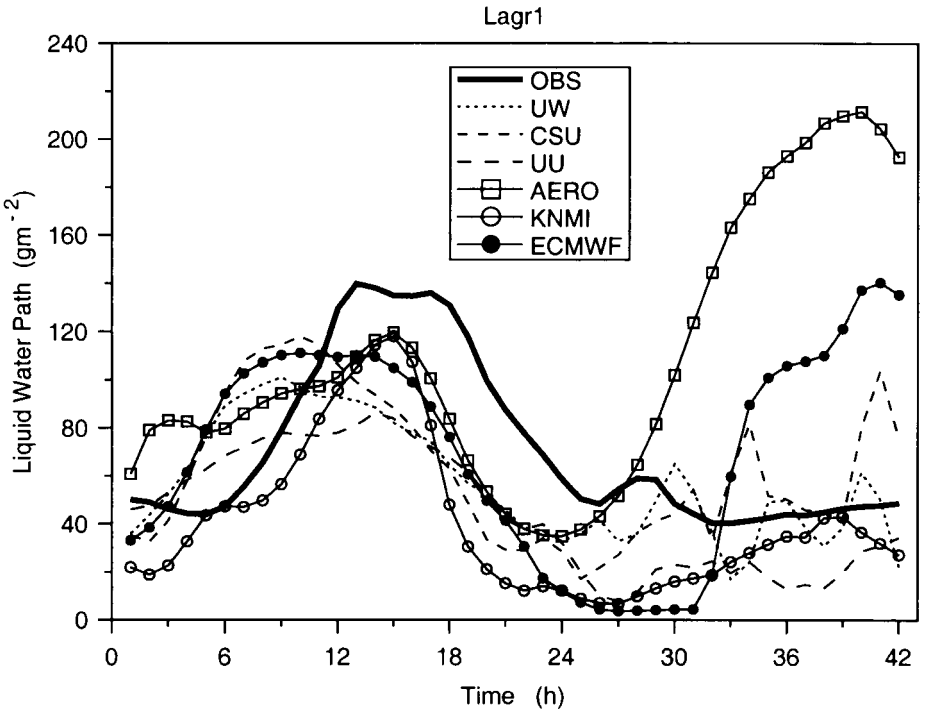

Figure 10. Liquid water path for the six models, and from the hourly-interpolated observed soundings.

cooling within the boundary layer is also a prime driver of the boundary-layer convection.

As discussed in Section 3.1.2, the radiative transfer schemes employed by the models differed considerably. Even with the same cloud properties, we might anticipate some differences in the predicted radiative fluxes. The differences in cloud properties between models can also have a considerable impact on the radiative fluxes. How large an impact on the top-of-atmosphere, boundary layer, and surface radiation balances did these differences have?

Figure 12 shows the shortwave and longwave radiative flux components at the top of the model domain (3 km) for all models except ECMWF, which did not supply any radiation fields. Satellite images did not show any cloud above the boundary layer over the L1 trajectory, so all models except UW computed the downwelling flux components at 3 km assuming clear-air radiative transfer above 3 km. The UW model did not compute radiative fluxes above 3 km. Instead, the water vapour path above 3 km was taken as a boundary condition, and radiative fluxes at 3 km were calculated by distributing this overlying water vapour in a single isothermal layer. The water vapour path was chosen to match the downwelling longwave radiation at 3 km to a fit from L1 aircraft observations analyzed by Austin and Bretherton (1997).

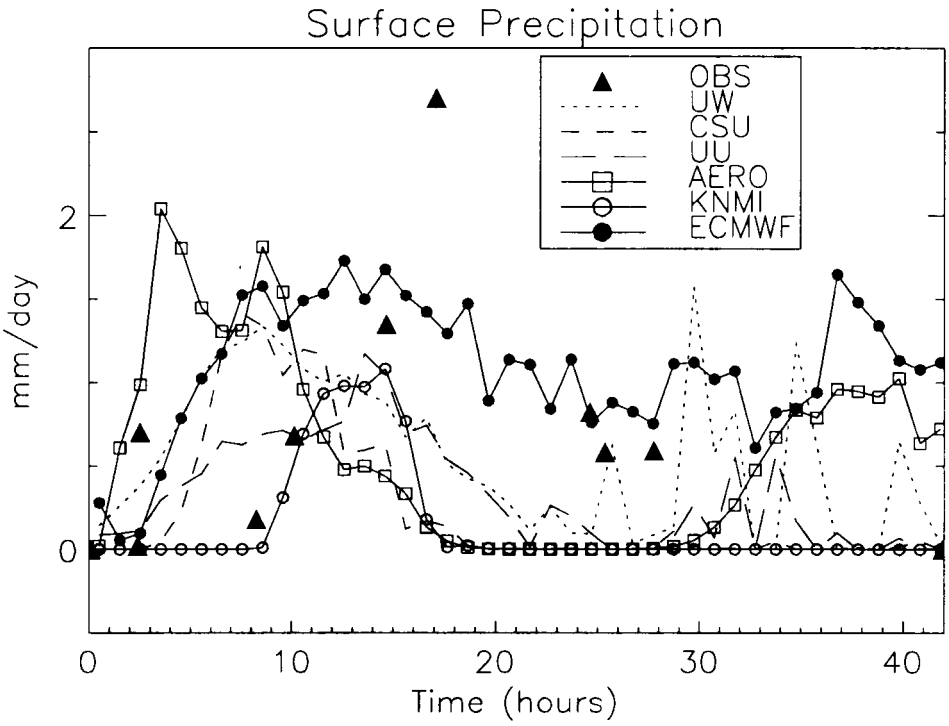

Figure 11. Surface precipitation rate for the six models, and from observations taken from aircraft legs at the stratocumulus cloud level at 150 m or less above the surface.

There was fair agreement in the downwelling longwave fluxes, with 20–30 W m^{-2} systematic differences between models. Surprisingly large differences (almost 10%) in the downwelling shortwave radiation at 3 km were found. The upwelling longwave fluxes were very similar for the first 20 hours, when all models were predicting complete cloud cover. Later in L1, simulations with smaller cloud fraction predicted up to 20 W m^{-2} higher upwelling longwave flux. The upwelling shortwave fluxes varied much more between models. The predicted 'albedo' (ratio of downwelling to upwelling fluxes at 3 km) at hour 21 varied from less than 20% (UW, CSU, KNMI) to 30% (AERO, UU). Figure 13 shows a scatterplot of hour 15 (early morning) and hour 21 (near local noon) albedo vs. liquid water path. This figure shows that most of the difference in the model albedos was associated with differences in their domain-averaged liquid water path. There is some residual scatter, which may be partly clue to the differences in the horizontal distribution of condensate within the domain, but also reflects differences in the radiation schemes used in the models. In particular, the hour 15 albedo from the UW model is quite low. Not all of these differences reflect legitimate scientific uncertainty in how cloud-radiation interaction should be parameterized. Since these simulations were conducted, a mistake in the scattering coefficient used in the UW radiation code

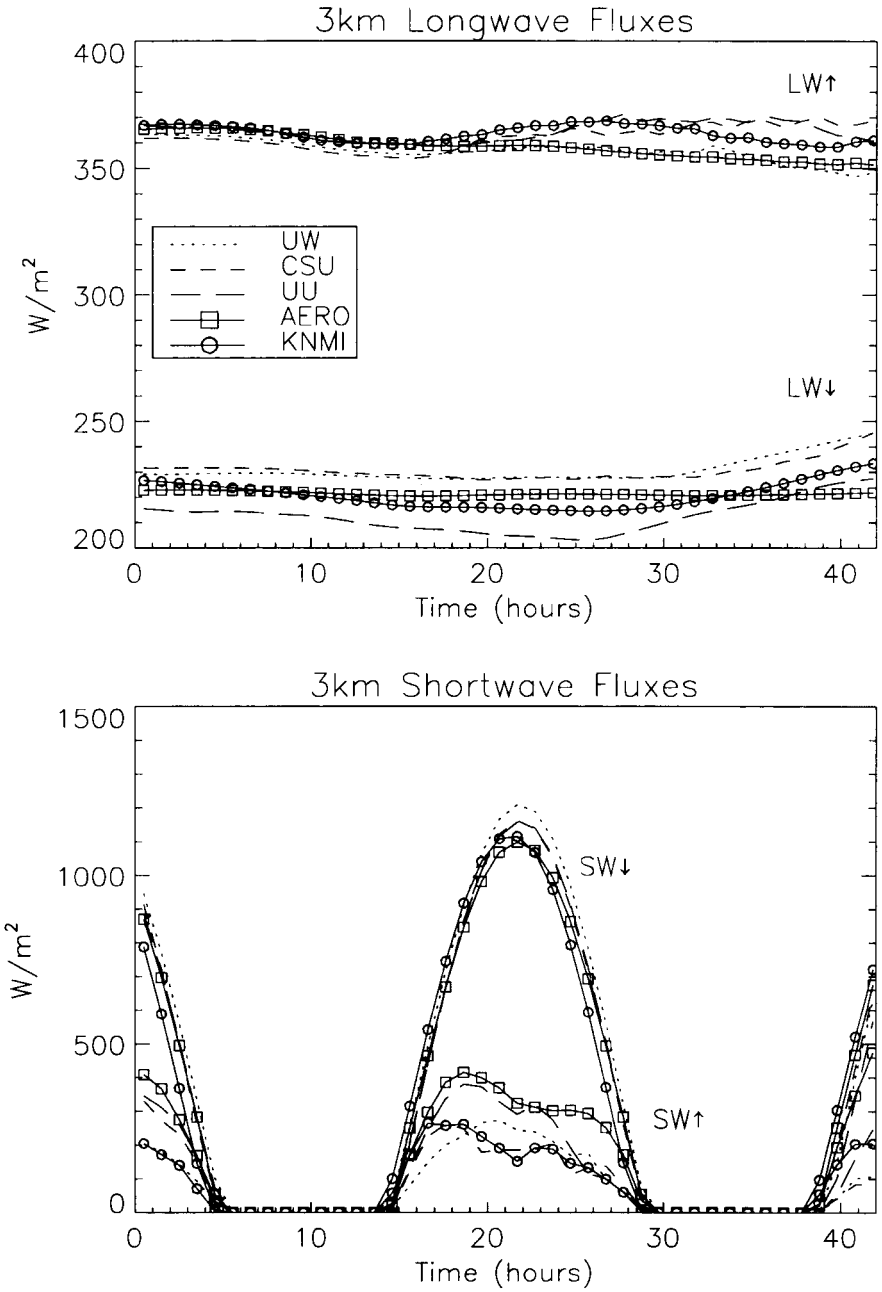

Figure 12. Upward and downward radiative fluxes at 3 km for all models except ECMWF. Top – longwave, bottom – shortwave. The dotted (UW) downwelling longwave fluxes are a fit to aircraft observations.

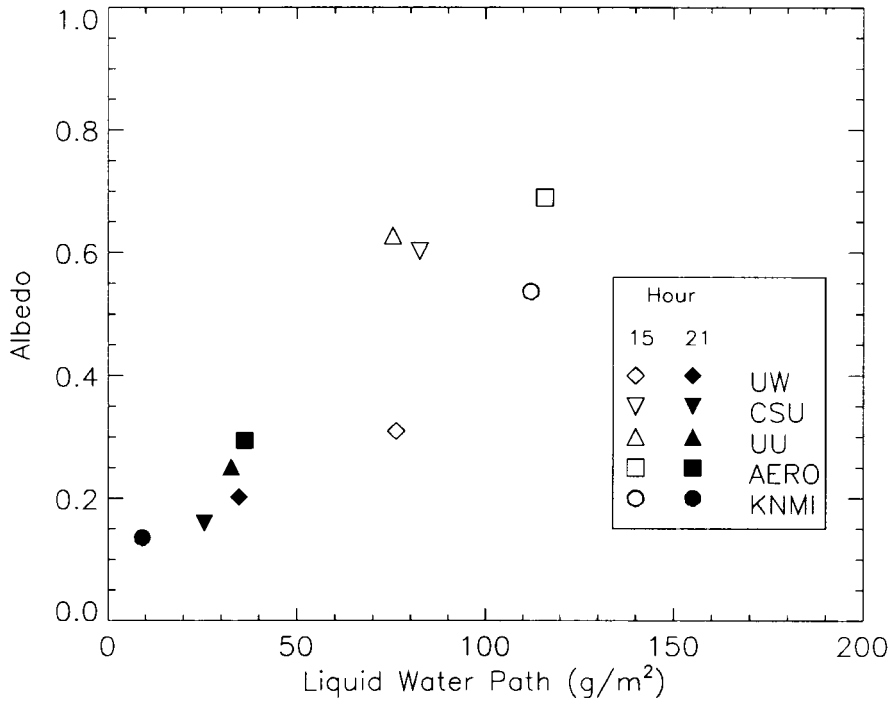

Figure 13. Scatterplot of albedo at 3 km vs. LWP at 15 (open symbols) and 21 hours (filled symbols) for all models except ECMWF.

was discovered that caused the albedo to be considerably underestimated, and would raise the UW albedos by around 0.2. In addition, the UW model treats solar radiation as being diffuse, leading to an albedo that is independent of zenith angle, while other models show an increase of almost 0.2 in albedo at the large solar zenith angles of early morning such as found at hour 15, which corresponds to a local time of 0700). While the UW shortwave radiation scheme has since been improved, sensitivity studies showed that the changes have little effect on the shortwave absorption within clouds. Since SST is specified, it is only the radiative flux divergence due to shortwave absorption that enters the boundary-layer dynamics. Hence, we do not believe that the UW run presented was affected by the shortcomings in the radiation scheme.

The model differences in radiative fluxes, driven mostly by the albedo differences, led to predictions of surface and top-of-atmosphere cloud radiative forcing that varied by as much as 100%. We have not considered the impact of using three-dimensional eddy-resolving models in place of two-dimensional models, nor have we examined the effects of grid resolution in the study, both of which may also have considerable effects on cloud properties in this type of transitional cloud regime. Without better agreement between the radiation schemes used in current LES

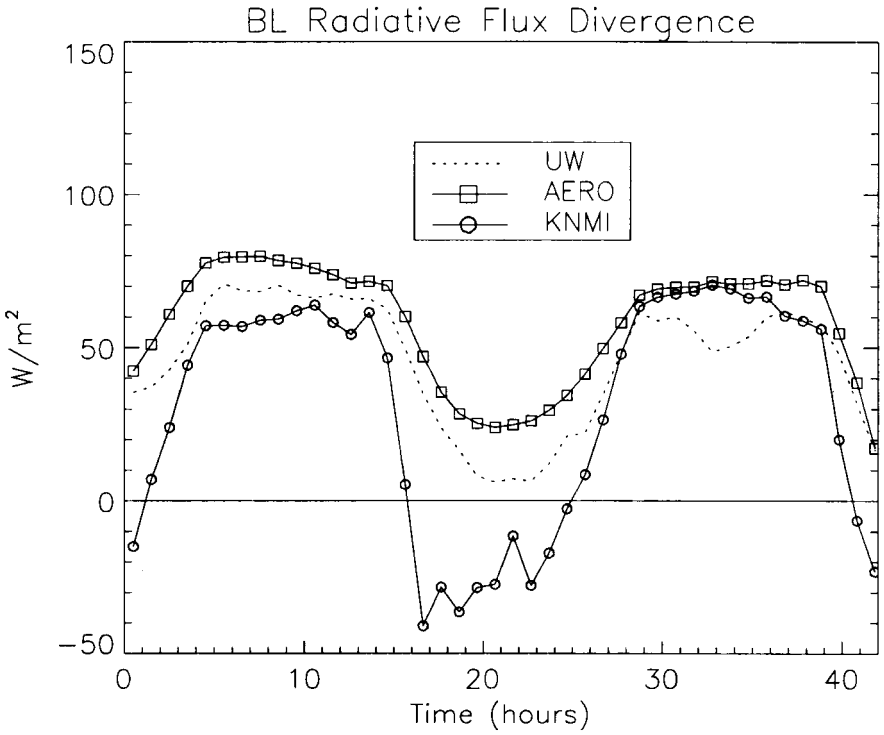

Figure 14. Net radiative flux divergence between the surface and 50 m above the mean inversion height for selected models.

models, the models cannot be expected to reproduce quantitatively these important climate forcings if considerable MBL cloud is present.

For the present study, the feedbacks of radiative flux divergence on the MBL convection are particularly important. The most important effects are cloud-top longwave cooling and in-cloud solar absorption. While the profiles of these quantities did differ somewhat between simulations, the single most important feedback on MBL dynamics is through the overall net radiative flux divergence integrated across the boundary layer. This is shown in Figure 14. Unfortunately, the flux divergence computed in the UU and CSU models was over a different height range than intended, so only results from the UW, AERO and KNMI models are shown. All simulations showed a prominent diurnal cycle. During the night, the flux divergence was due purely to longwave cooling, and all three models predicted similar 60–75 W m^{-1} flux divergences. The difference between the nighttime and noontime (hour 21) values measures the heating due to solar absorption integrated across the MBL, which occurs primarily in clouds. The AERO and UW models had about 50 W m^{-2} MBL-integrated solar absorption, while the KNMI model had 80–90 W m^{-2} of solar absorption despite having a similar noontime liquid water path to AERO.

These differences reflect substantial differences between the models in the total absorption of shortwave radiation in the cloud layer. To explore these differences, we compared the absorption computed by the models with the initial profiles of vapour mixing ratio and liquid water, with the sun at zenith angles of 0° and 60°. To ensure that differences were not created by interpolation of these profiles onto different model grids, the radiation schemes were all run with the same grid spacing of 10 hPa.

The absorption and the albedo at cloud top from the radiation schemes of the different models, with the sun at zenith, are shown in Table III. The cloud layer absorption in the KNMI model was almost four times as large as in the AERO model; the CSU model also had very large absorption, with the UU and UW models having absorptions slightly larger than AERO. Reliable measurements of absorption are very difficult to obtain from aircraft data, so no comparison with observed fluxes is attempted here. However, we can compare these models with more detailed and computationally intensive radiative transfer schemes that have been optimized to best match highly spectrally resolved (line-by-line) laboratory data, such as the Slingo and Schrecker (1982) 24-band shortwave scheme. Results using this scheme, also shown in Table III, suggest a higher albedo than all models, and an absorption slightly larger than in AERO, UU and UW, but much lower than in CSU and KNMI. The high absorption by the CSU radiation scheme has since been traced to use of an incorrect weighted average of the droplet absorptivity over the different wavelengths within each of the six bands used by the scheme (J. Harrington, 1997, personal communication). It would be interesting/to test the sensitivity of the CSU model's simulation to an update of the CSU radiation scheme, but this was not done for this intercomparison.

These model-to-model differences in absorption should be of considerable dynamical significance. More solar absorption promotes cloud breakup during the day and reduces the net radiative cooling in the boundary layer averaged over the diurnal cycle, which is the main driver of turbulence and entrainment. This would probably have led to much more noticeable differences between model results were the L1 case not so strongly forced by advection over rapidly increasing SST, which also stimulates boundary-layer turbulence. More reassuringly, all models did predict comparable cloud-top albedo (ratio of upwelling to downwelling solar radiation) with the sun at zenith, though the UW model considerably underestimated albedo at large solar zenith angles (not shown).

4.3. SURFACE FLUXES

The wind speed in all models except AERO was relaxed to the observations. Thus, the modelled surface latent and sensible heat fluxes, shown in Figure 15, were mainly sensitive to the model-predicted air–sea temperature and humidity jumps, as well as the exact flux parameterization used. The modelled latent and sensible heat fluxes were compared with observed surface fluxes derived from near-surface

TABLE III

Total shortwave absorption in the cloud layer and albedo at cloud top with the hour zero water vapour and mixing ratio profiles, and the sun at zenith, for all models except ECMWF, and the Slingo and Schrecker (1982) 24-band radiative transfer scheme.

Acronym	Absorption ($W\ m^{-2}$)	Albedo (%)
AERO	48	40
KNMI	186	42
CsU	113	43
UU	54	39
UW	60	37
Slingo	68	48

(30 m above sea level during the day and 150 m during the night) aircraft flight legs. The observed fluxes were estimated by BAS95 using a bulk aerodynamic formula applied to the leg-mean air–sea temperature and moisture differences. De Roode and Duynkerke (1997) used an eddy correlation method to derive the fluxes.

The observed sensible heat fluxes derived from the bulk aerodynamic and eddy correlation methods are generally consistent. The sensible heat fluxes from all models were quite similar to these observations. At the beginning of L1, the air temperature was observed and initialized in the models to be almost 1 K warmer than the SST. After a few hours, the air temperature in all models cooled to a fraction of a kelvin above the SST, and the sensible heat fluxes became small. As the SST started to rise rapidly, the air temperature lagged 1–2 K behind the SST in all models, producing a maximum in sensible heat flux (particularly pronounced in the ECMWF model) and a rapid rise in latent heat flux. As the air column exited the zone of strong SST gradient over the Azores Current, the sensible heat flux decreased in the models and observations.

The observed latent heat fluxes derived from the bulk aerodynamic and eddy correlation methods evolve similarly, but the bulk method predicts latent heat fluxes that are at least twice as large as with the eddy correlation method over most of L1, for reasons that are not well understood. All models except AERO reproduced the latent heat flux evolution quite well, and were bracketed between the observed eddy-correlation and bulk flux measurements. The latent heat fluxes ramped up rapidly during the period of rapid SST increase. Surprisingly, the AERO model had considerably lower latent heat fluxes than were observed, despite surface wind

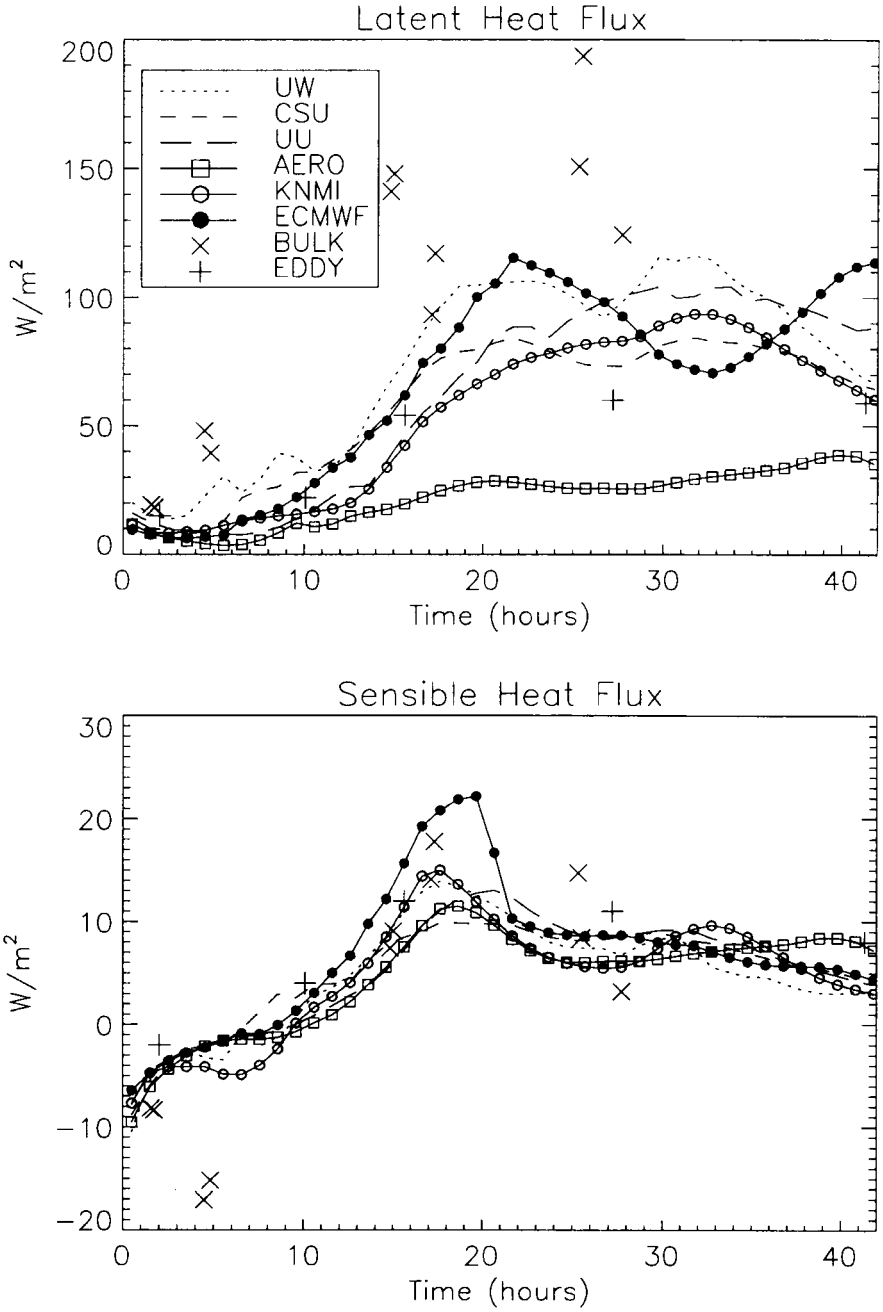

Figure 15. Sensible and latent heat fluxes at the lowest grid level in the six models, and from bulk aerodynamic formulae (BULK, from BAS95) and eddy correlation (EDDY, from de Roode and Duynkerke (1997)) applied to the wind and temperature observations taken from the lowest-level aircraft legs. Each EDDY flux is the average over all lowest legs in one of the five Electra and C130 flights.

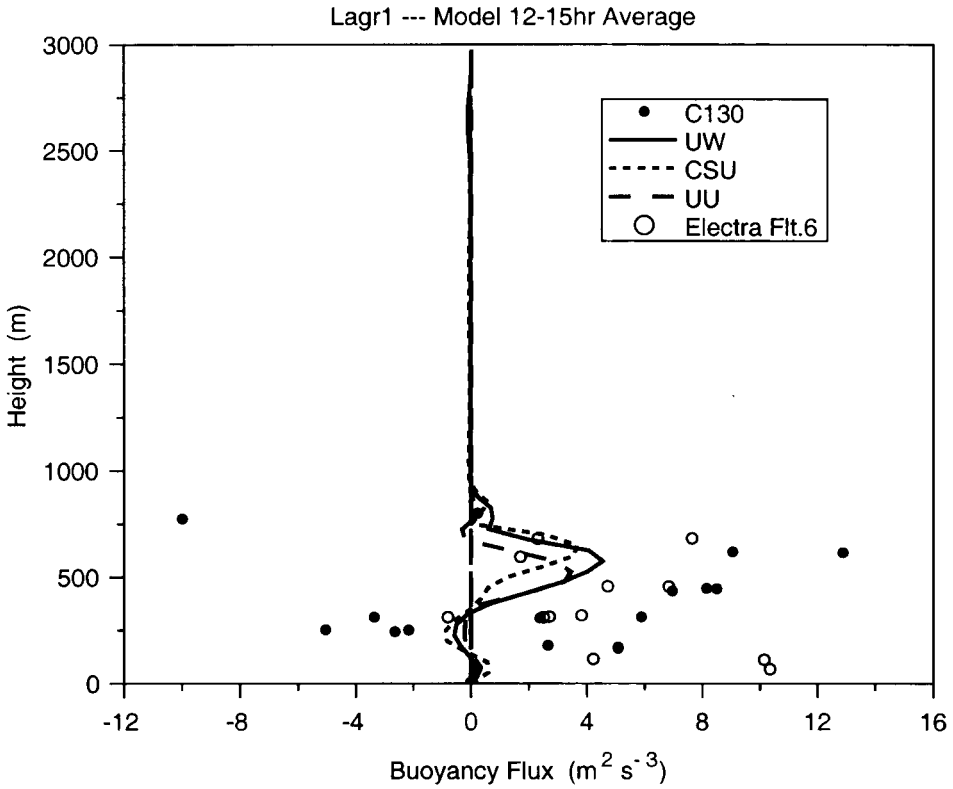

Figure 16. Buoyancy fluxes averaged over hour 15 for the six models, and aircraft observations of buoyancy flux from the C130 (hours 9–12, from Duynkerke et al. (1995)), and the Electra (hours 13–18, provided by Dr. Q. Wang).

speeds that were comparable to the observations and near-surface mixing ratios that were lower than observed.

4.4. CONVECTIVE TURBULENCE STATISTICS

Lastly. we compare model estimates of buoyancy fluxes and turbulence with observations. These were only archived for the 2D models, since some 1D models do not predict these quantities. The buoyancy flux was the dominant source of turbulent kinetic energy (TKE) during L1. Figure 16 shows the buoyancy flux for the three 2D models at hour 15, which corresponds approximately to the time of the observational analysis of DeRoode and Duynkerke (1996). The profiles predicted by the three models were quite similar, with weak negative buoyancy fluxes below cloud base and positive buoyancy fluxes within the cloud layer. The observations had considerable scatter, but suggest that buoyancy fluxes were stronger in the cloud layer than predicted by the models.

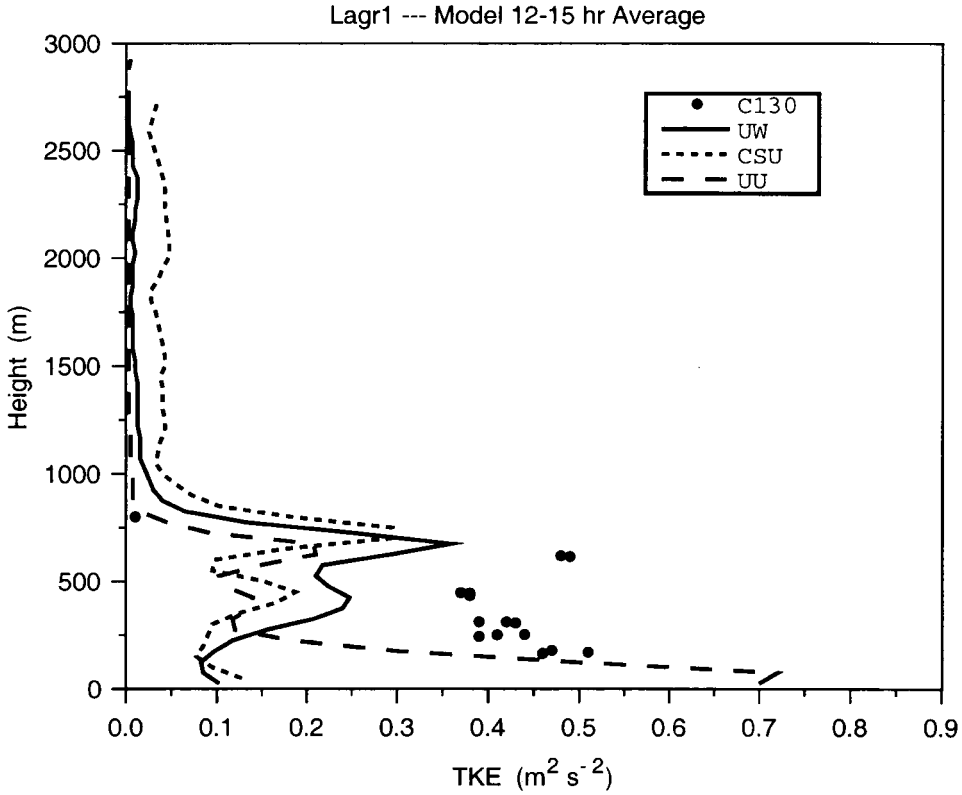

Figure 17. TKE averaged over hour 15 for the three 2D models, and hour 9–12 C130 observations from Duynkerke et al. (1995).

Figure 17 shows the corresponding profiles of TKE. The CSU model predicted a surprisingly large TKE above the boundary layer, and the UU model predicted very high values of TKE near the ground, but the three models predicted similar TKE profiles through most of the boundary layer, with a maximum near the top of the MBL. The observations of DeRoode and Duynkerke (1996) showed uniform and higher TKE throughout the MBL. Recent studies have shown that 2D models have a systematic bias toward higher TKE than 3D models given the same radiative forcing (Moeng et al., 1996); this would exacerbate the differences between models and observations. These differences may have to do with the effects of drizzle on the MBL dynamics, whose details were not possible to observe in the field with accuracy. Were the area-averaged drizzle being overestimated by the models at this time, this would cause an overestimate of latent heating in the cloud layer and a decrease in the buoyancy fluxes compared to the observations. Perhaps the interaction of mesoscale circulations with drizzle, not represented within the limited domain of the 2D model, might decrease drizzle rate and increase TKE.

Observations of TKE late in L1, when the boundary layer had become cumulus-coupled, matched the 2D models better (not shown), though the intermittency of the cumulus convection makes the comparison rather uncertain.

5. Sensitivity Studies

One of the authors (B. Stevens) conducted a number of sensitivity studies in order to better understand the role of various physical processes. Here we briefly discuss some of the results; further details can be found in Stevens (1996).

Sensitivity simulations with the CSU model suggest that, of the myriad forcings, the time variation of the lower boundary condition was largely responsible for affecting the change from solid cover in a shallow boundary layer (characteristic of easily times) to broken cloud cover in a deeper boundary layer (characteristic of later times). This picture, wherein the transition is forced by the time variation in sea-surface temperatures as the column is advected over warmer water, is in accord with previous theoretical work (Krueger et al., 1995; Wyant et al., 1997). Although the time variation in the SSTs appears to be the single most important physical effect, drizzle was also found to play an important role, as discussed below.

To better understand the role of drizzle, the CSU model was run as in the control case, but with all drizzle and droplet sedimentation suppressed. Figures 18 and 19 compare the evolution of this simulation (CSU-ND) with the control. CSU-ND showed a similar evolution to the control CSU simulation for the first 18 hours. with a single stratocumulus layer with maximum updraft strengths on the order of 1 m s^{-1} and a decrease in cloud fraction thereafter. However, there are some important differences. During the first 18 hours, the nonprecipitating boundary layer entrained more, deepening 200 m more than the control run by hour 15. This occurred because latent heating in the control run was stabilizing the boundary layer and suppressing convection. However, the nonprecipitating boundary layer still developed a thicker cloud with double the liquid water path of the control run. During this phase, there were interesting differences between the temperature, moisture and turbulence profiles in the control and noprecipitating cases, too. The nonprecipitating case maintained a more closely well-mixed structure and much more vigorous eddies than the control, which maintained about 1 K of stabilization in the subcloud layer due to evaporating drizzle.

After sunrise at hour 15, the nonprecipitating stratocumulus layer rapidly dissipated, presumably due to solar absorption in the thick cloud layer and decoupling. After hour 16, vertical velocity spikes of 2–3 m s^{-1} suggest intermittent cumulus convection originating in the subcloud layer. Between hours 18–19 the stratocumulus broke up entirely, and the remainder of CSU-ND was characterized by cloud fractions of 30% or less. In the control run, cloud fraction also decreased after hour 18, but took 10 hours before it fell below 30%. The onset of more vigorous ‘cumulus-like’ updrafts in the control run only occurred after hour 28. Without

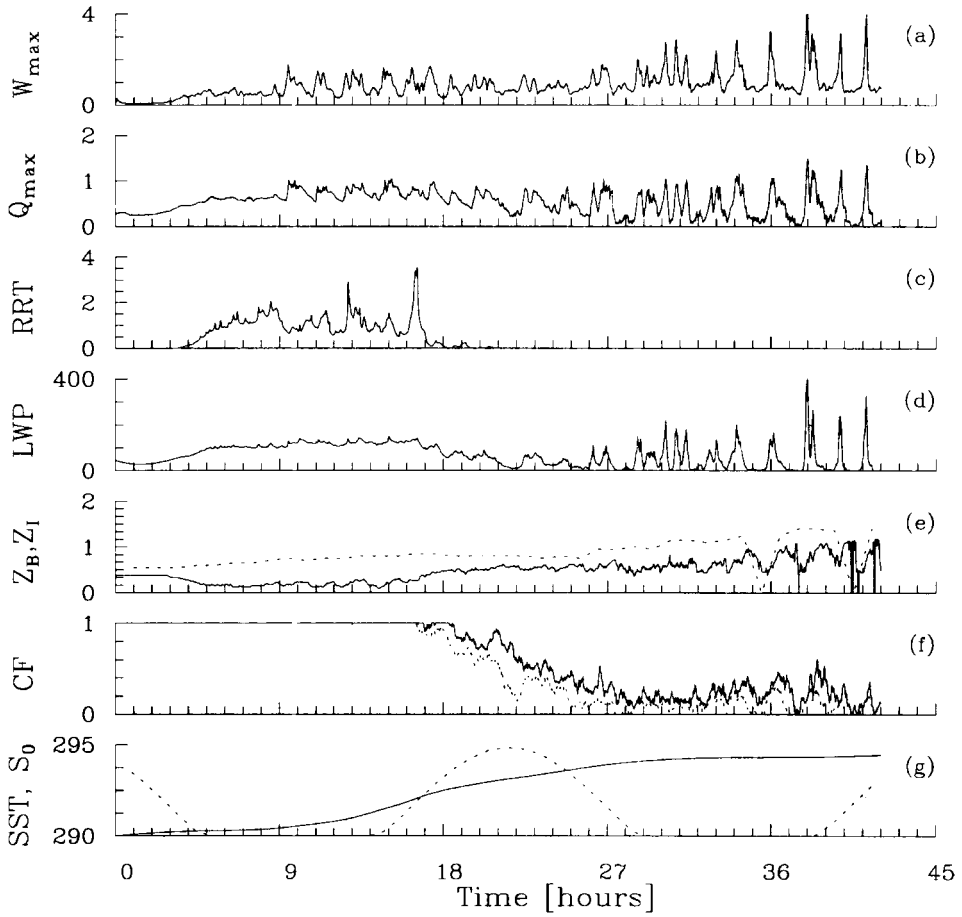

Figure 18. Selected time series for the control CSU simulation: (a) Maximum vertical velocity (m s^{-1}); (b) Maximum liquid water content (g kg^{-1}); (c) Surface rain rate (mm day^{-1}); (d) Liquid water path (g m^{-2}); (e) Horizontally averaged cloud base (solid) and top (dashed) in km, (f) Two measures of cloud fraction–fraction of columns with nonzero liquid water (solid) and with liquid water path exceeding 13 g m^{-2} (dashed), (g) SST (solid) and relative solar insolation (dashed).

much cloud, the boundary-layer radiative cooling and entrainment were reduced, and the boundary layer did not deepen further. Contrary to earlier suggestions based on simple bulk models (Albrecht, 1989; Pincus and Baker, 1994), suppression of drizzle reduced cloud fraction and entrainment during the second half of CSU-ND, compared to the control run.

Three-dimensional simulations of three hour periods during the first night of L1 were also conducted (Stevens, 1996). The 3D simulations support the basic conclusions garnered from the 2D simulations: drizzle tends to suppress turbulence, and as a result the PBL tends to entrain less and deepen less rapidly (Stevens et al., 1998).

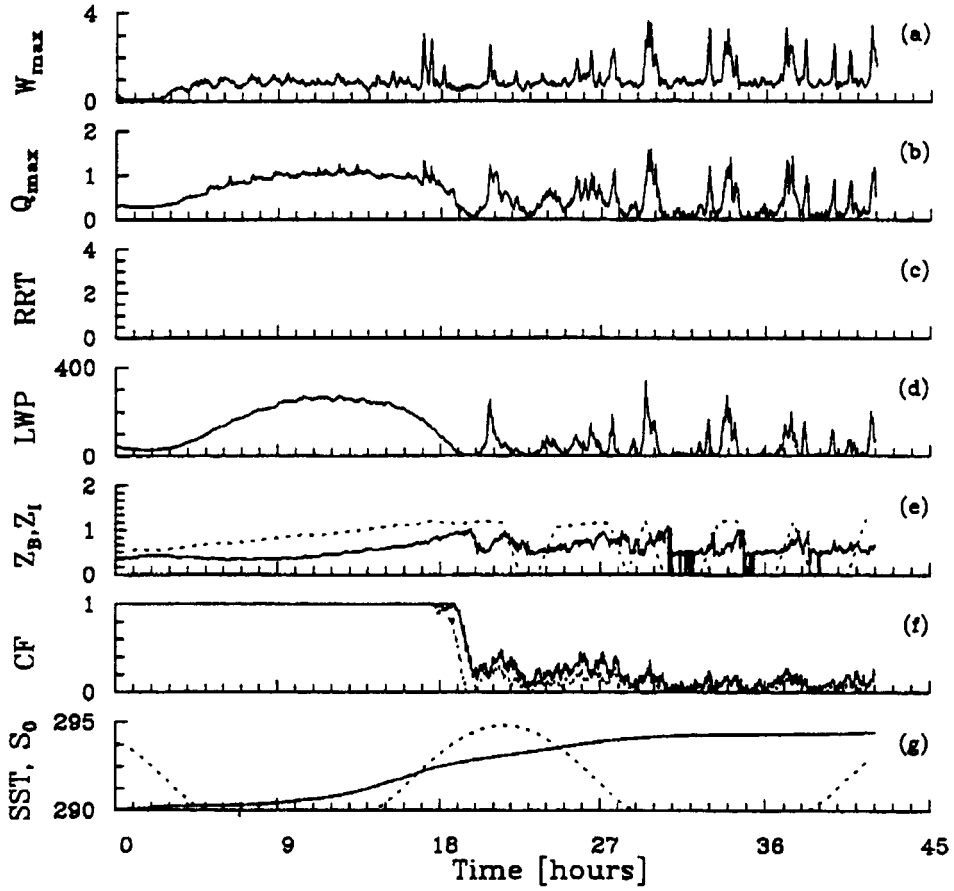

Figure 19. As in Figure 18, for the CSU-ND simulation.

6. ASTEX Lagrangian 2

The second ASTEX Lagrangian (L2) was also modelled at the same GCSS workshop. During L2, a boundary-layer air column with a shallow, weakly precipitating cumulus layer about 150 hPa deep capped with sporadic stratocumulus patches was tracked for almost two days (BP95; BAS95). The field observations during L2 were even more successful than in L1, since one of the tetroons released at the start of L2 was tracked throughout the experiment, and there were no gaps in aircraft coverage.

Three 1D models (KNMI, AERO, and ECMWF) and two 2 models (UU and UW) participated in this intercomparison. The models and observations did not agree nearly as well as in L1. All models did generate a cumulus-capped boundary-layer cloud, but most models (except KNMI) produced a considerably different

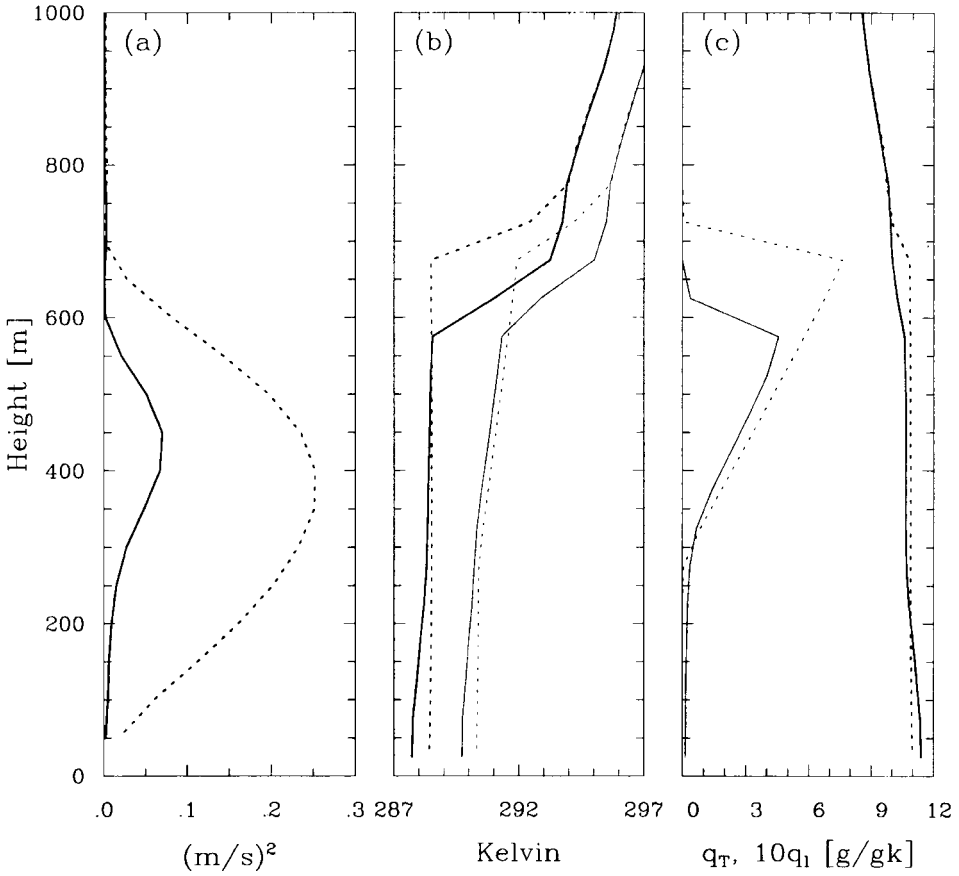

Figure 20. Profiles of horizontally averaged (a) Vertical velocity variance, (b) θ_l (thick) and θ_v (thin), (c) q^t (thick) and $10q_l$ (thin), averaged over the fifth hour of L1 for the CSU (solid) and CSU-ND (dashed) simulations.

evolution of the associated stratocumulus cloud amount than was observed, with much less cloud during day 1 and much more cloud on day 2 than was observed.

Later sensitivity studies of Wyant (1997) for L2 suggest that the modelled cloud fraction evolution was quite sensitive to the specified mean vertical motion profile, and that better agreement between one model and observations could be achieved by specifying less subsidence earlier in L2 and more subsidence later in L2 than originally suggested in BAS95. The observations of mean vertical motion discussed in BAS95 are uncertain enough to easily allow for this possibility. In addition, satellite retrievals of cloud fraction from Martin et al. (1995) suggest that the cloud cover varied considerably over a 100 km scale, so that the aircraft observations, which spanned a 60 km wide Lagrangian column, may not be representative of a broader region. In particular, the cloud observed late in day 1 of L2 appeared to be concentrated in the boundary-layer air column, and

surrounding air columns had much lower cloud fraction. Hence, the GCSS participants decided that the observed large-scale forcings did not sufficiently constrain the cloud evolution to provide a meaningful test of the cloud models. For these reasons, we are not planning to publish the results from this intercomparison. However, with these caveats, other modellers are encouraged to use the modellers' dataset for L2 available through the GCSS Working Group 1 home page (www.atmos.Washington.edu/∼breth/GCSS/GCSS.html), and we may revisit the L2 data set in future.

7. Conclusions

This GCSS intercomparison study compared 1D and eddy-resolving 2D boundary-layer models with multiday Lagrangian observations of a well-observed cloud-topped MBL. The models were forced with observed time-varying surface and above-boundary layer conditions, observed mean vertical motion and horizontal winds. The participating 2D and 1D models qualitatively represented the MBL evolution fairly well, including the deepening of the inversion, the associated change from a shallow, well-mixed stratocumulus-capped MBL to a cumulus-coupled MBL, and the general evolution of cloud fraction and liquid water path. Surface fluxes were also fairly realistic, but this is to be expected since the model winds were continuously relaxed toward observed values. A day-long period of light drizzle was observed. Surprisingly, despite diverse microphysical parameterizations, most models predicted reasonable surface precipitation rates during this period. We believe, based on our combined experience, that modelled precipitation rates from boundary-layer clouds are usually more sensitive to the microphysical parameterization than the current study suggests. The relative insensitivity found here may be associated with a very moist overlying troposphere, which largely suppressed drying of the MBL due to entrainment and rendered precipitation the primary sink of moisture available to balance surface fluxes.

There was significant model-to-model variability in radiative fluxes, even between the eddy-resolving models. Even when all the radiative parameterizations used in the different models were all applied to a single profile with a 300-m thick stratus cloud, the solar absorption within clouds differed by almost a factor of four between models. These parameterizations also produced much less spectacular, but significant, differences in albedo. The longwave radiation parameterizations produced up to 20 W m^{-2} differences in downwelling longwave radiation at cloud top. Both shortwave absorption and MBL-top downwelling longwave radiation affect the turbulent circulations of the MBL, feeding back on the cloud properties themselves. This emphasizes the need for eddy-resolving models to incorporate more accurate, well tested radiation parameterizations before they can be used to draw quantitatively reliable conclusions about cloud-radiation-climate feedbacks. The turbulent character of the boundary-layer convection was qualitatively well

represented within the 2D models, but the model-predicted turbulent kinetic energy was somewhat lower than observed during the drizzling stratocumulus phase of the evolution. Since 2D models have different turbulence statistics than 3D models, detailed comparison of the structure of the convection probably should await a 3D eddy-resolved simulation. Furthermore, the simulation should encompass a domain with a width of at least 10 km, so that the interaction of drizzle with mesoscale structure that was observed during this part of L1 can be better accounted for.

While the 2D models were more similar in evolution to each other than to the 1D models, and could probably be used to improve parts of the 1D models, the 1D models performed acceptably given the complexity of the observed MBL dynamics. We are currently not at a point at which eddy-resolved models can be considered equivalent to observations for the purpose of improving 1D models.

For most climatologically important cloud-topped MBL types, including mid-latitude marine stratus and trade cumulus, we currently do not have adequate integrated datasets for the type of comprehensive model-data comparisons presented in this paper. Even in the case presented, observational uncertainties complicated the interpretation of this comparison. The Lagrangian framework was successful in removing one major source of uncertainty (horizontal advection) from a model-data intercomparison, but despite considerable efforts vertical advection (or equivalently, entrainment rate) remained a major source of observational uncertainty in both ASTEX Lagrangians. In particular, our less successful attempt to model L2 suggested that it is necessary to specify the variations of vertical advection reliably with timescales of a few hours and space scales of 100 km to constrain the detailed evolution of the clouds within a column that can be surveyed by aircraft. This might dictate use of an Eulerian column in future experiments, for which a mesoscale array of surface-based remote sensing such as mm-wave radars, microwave and broadband radiometers, and profilers can better complement the aircraft observations to provide the large-scale advection and statistical distributions of some cloud and boundary-layer properties. In particular, the 1999 GCSS Boundary Layer Working Group intercomparison focussed on a continental shallow cumulus-topped boundary layer from the Oklahoma site of the Atmospheric Radiation Measurement program, for which a data set of this type is now available.

Acknowledgements

We thank Dr. Qing Wang of the Naval Postgraduate School for providing NCAR Electra turbulent flux data used in Figure 16. We also thank Aad van Ulden and our participants from KNMI and IMAU for hosting the workshop that inspired this paper. Funding for this work was provided by many sources, including grants NASA NAG1-1711 (Bretherton, Wyant), ONR grant N00014-91-J-1175 (Krueger), and grants from program PATOM/INSU and computer resources from IDRIS, France (Bechtold).

Appendix A. Construction of Hourly Profiles from Aircraft Soundings and ECMWF Analyses

The hourly aircraft-derived soundings were calculated as follows:

1. In each sounding j at time t^j, we found an inversion base pressure p_i^j corresponding to a local minimum in temperature below the inversion.
2. Based on the radar altimeter elevation and the measured pressure at the bottom of the sounding, the sounding was hydrostatically extrapolated down to the sea-level pressure p_s^j assuming that potential temperature, mixing ratio and winds were the same as at the lowest sounding level (which is usually at 15–30 m during the day and 100 m at night).
3. The tops of the aircraft soundings were typically 20–150 hPa above the MBL capping inversion. The ECMWF analysis along the trajectory was used to extrapolate above the top of each aircraft sounding, producing a complete column sounding from the surface up to 100 hPa.
4. An hourly sounding of a variable $f(p, t)$ at a time t is found using the weighted average of the column soundings

$$f(p,t) = \sum_{j=k-n_L+1}^{k+n_R} w^j f(\zeta^j(p)). \tag{1}$$

Here k is the index of the last aircraft sounding before t. The soundings j used in the average are found by first looking for soundings within a time interval Δt = 3 hrs of t. If there are several soundings in between $t - \Delta t$ and t, then all n_L of them are used in the weighted average. Otherwise the last sounding prior to t is used, whether or not it falls in this time interval, and n_L = 1. Similarly, if there are several soundings in the three hours after t, all n_R of them are used in the weighted average. Otherwise the first sounding after t is used, and n_R = 1.

The averaging procedure is designed to preserve inversion sharpness. We first calculate weighted average inversion and surface pressures at time t:

$$p_i(t) = \sum_{j=k-n_L+1}^{k+n_R} w^j p_i^j, \tag{2}$$

$$p_s(t) = \sum_{j=k-n_L+1}^{k+n_R} w^j p_s^j, \tag{3}$$

We introduce a scaled pressure $\zeta^j(p)$ so that the surface and inversion base pressures in sounding j are scaled into those at t. Above p_f = 700 hPa we do not rescale the pressure. Between the inversion base and p_f a linear scaling that matches between these two scalings is used. Thus,

$$\chi(p) = \frac{p - p_i}{p_s - p_i}, \tag{4}$$

$$\zeta^j(p) = \chi(p) p_s^j + (1 - \chi(p)) p_i^j, (p_s > p > p_i), \tag{5}$$

$$\chi(p) = \frac{p - p_f}{p_i - p_f}, \tag{6}$$

$$\zeta^j(p) = \chi(p) p_i^j + (1 - \chi(p)) p_f, (p_i > p > p_f), \tag{7}$$

$$\zeta^j(p) = p, (p_f > p). \tag{8}$$

The weights w^j are uniquely specified by the following constraints. First they must sum to one,

$$\sum_{j=k-n_L+1}^{k+n_R} w^j = 1. \tag{9}$$

Second, they give a weighted average sounding time equal to t,

$$\sum_{j=k-n_L+1}^{k+n_R} w^j t^j = 1. \tag{10}$$

Third, if there are multiple soundings between $t - \Delta t$ and t ($n_L > 1$), then a triangular weighting function maximum at t and zero at $t - \Delta t$ is used to choose the relative weight of each sounding. An analogous procedure is used if $n_R > 1$:

$$\text{If } n_L > 1, w^j/w^k = \frac{t^j - t + \Delta t}{t^k - t + \Delta t}, (k - n_L + 1 \leq j < k), \tag{11}$$

$$\text{If } n_R > 1, w^j/w^{k+1} = \frac{t^j - t - \Delta t}{t^k - t - \Delta t}, (k + 1 < j \leq k + n_R). \tag{12}$$

5. Lastly, the temporally averaged hourly sounding is vertically averaged over 10 hPa increments up to 700 hPa. Above 700 hPa, the sounding is given at the ECMWF-supplied pressure levels (650, 600, 550, 500, 400, 300, 200, 100 hPa).
6. The hourly sounding files of winds, temperature, vapour mixing ratio and liquid water mixing ratio are available as part of the ASTEX Lagrangian modellers data set on the WWW at the URL http://www.atmos.washington.edu/∼breth.

References

Albrecht, B. A.: 1989, 'Aerosols, Cloud Microphysics and Fractional Cloudiness', *Science* **245**, 1227–1230.

Albrecht, B. A., Bretherton, C. S., Johnson, D., Schubert, W., and Frisch, A. S.: 1995: 'The Atlantic Stratocumulus Transition Experiment (ASTEX), *Bull. Amer. Meteorol. Soc.* **70**, 889–903.

Austin, P. H. and Bretherton, C. S.: 1997, 'Broadband Radiative Fluxes during the ASTEX Lagrangian Experiments'. University of British Columbia Atmospheric Science Programme Technical Report No. 44, 33 pp. Available on WWW at ftp://ftp.geog.ubc.ca/atsci/reports, or from Dr. P. H. Austin, Atmospheric Science Programme, Geography 217, UBC, 1984 West Mall Vancouver, BC, V6T 1Z2, Canada.

Bechtold, P., Krueger, S. K., Lewellen, W. S., van Meijgaard, E., Moeng, C.-H., Randall, D. A., van Ulden, A., and Wang, S.: 1996: 'Modeling a Stratocumulus-Topped PBL: Intercomparisons among Different 1D Codes and with LES', *Bull. Amer. Meteorol. Soc.* **77**, 2033–2042.

Bretherton, C. S., Austin, P. H., and Siems, S. T.: 1995: 'Cloudiness and Marine Boundary Layer Dynamics in the ASTEX Lagrangian Experiments. Part II: Cloudiness, Drizzle, Surface Fluxes and Entrainment', *J. Atmos. Sci.* **52**, 2724–2735.

Bretherton, C. S. and Pincus, R.: 1995, 'Cloudiness and Marine Boundary Layer Dynamics in the ASTEX Lagrangian Experiments. Part I: Synoptic Setting and Vertical Structure', *J. Atmos. Sci.* **52**, 2707–2723.

Bretherton, C. S., MacVean, M. K., and 14 coauthors, 1999: 'An Intercomparison of Radiatively Driven Entrainment and Turbulence in a Smoke Cloud, as Simulated by Different Numerical Models', *Quart. J. Roy. Meteorol. Soc.* **125**, 391–423.

CCM3, 1997: CCM3 Validation of Total Cloud, in the NCAR Community Climate Model WWW site (http://www.cgd.ucar.edu:80/cms/ccm3).

Deardorff, J. W.: 1972, 'Parameterization of the Planetary Boundary Layer for Use in General Circulation Models', *Mon. Wea. Rev.* **100**, 93–106.

Del Genio, A. D., Yao, M.-S., Kovari, W., and Lo, K. K.-W.: 1996, 'A Prognostic Cloud Water Parameterization for Global Climate Models', *J. Climate* **9**, 270–304.

de Roode, S. R. and Duynkerke, P. G.: 1996, 'Dynamics of Cumulus Rising into Stratocumulus as Observed during the First "Lagrangian" Experiment of ASTEX', *Quart. J. Roy. Meteorol. Soc.* **122**, 1597–1623.

de Roode, S. R. and Duynkerke, P. G.: 1997, Observed Lagrangian Transition of Stratocumulus into Cumulus during ASTEX: Mean State and Turbulence Structure', *J. Atmos. Sci.* **54**, 2157–2173.

Duynkerke, P. G., Zhang, H.-Q., and Jonker, P. J.: 1995, 'Microphysical and Turbulent Structure of Nocturnal Stratocumulus during ASTEX', *J. Atmos. Sci.* **52**, 2763–2777.

Fowler, L. and Randall, D. A.: 1996,' Liquid and Ice Microphysics in the CSU General Circulation Model. Part II: Impact on Cloudiness, The Earth's Radiation Budget, and the General Circulation of the Atmosphere', *J. Climate* **9**, 530–560.

GEWEX Cloud System Science Team: 1993, 'The GEWEX Cloud System Study (GCSS)', *Bull. Amer. Meteorol. Soc.* **74**, 387–399.

Hartmann, D. L., Ockert-Bell, M. E., and Michelsen, M. L.: 1992, 'The Effect of Cloud Type on the Earth's Energy Balance', *J. Climate* **5**, 1281–1304.

Holtslag, A. A. M. and Boville, B. A.: 1993, 'Local Versus Nonlocal Boundary-Layer Diffusion in a Global Climate Model', *J. Climate* **6**, 1825–1842.

Klein, S. A. and Hartmann, D. L.: 1993, 'The Seasonal Cycle of Low Stratiform Clouds', *J. Climate* **6**, 1587–1606.

Krueger, S. K., McLean, G. T., and Fu, Q.: 1995, 'Numerical Simulations of the Stratus to Cumulus Transition in the Subtropical Marine Boundary Layer. Part 1: Boundary Layer Structure', *J. Atmos. Sci.* **52**, 2839–2850.

Martin, G. M., Johnson, D. W., Rogers, D. P., Jonas, P. R., Minnis, P., and Hegg, D. A.: 1995: 'Observations of the Interaction between Cumulus Clouds and Warm Stratocumulus Clouds in the Marine Boundary Layer during ASTEX', *J. Atmos. Sci.* **52**, 2902–2922.

McClatchey, R. A.: 1972, *Optical Properties of the Atmosphere, Third Edition*, U.S. Air Force Office of Research Publication AFCRL-72-0497.

Moeng, C.-H., Cotton, W. R., Bretherton, C. S., Chlond, A., Khairoutdinov, M., Krueger, S., Lewellen, W. S., MacVean, M. K., Pasquier, J. R. M., Rand, H. A., Siebesma, A. P., Sykes, R. I., and Stevens, B.: 1996: 'Simulation of a Stratocumulus-Topped PBL: Intercomparison among Different Numerical Codes', *Bull. Amer. Meteorol. Soc.* **77**, 261–278.

Morcrette, J.-J., 1991: 'Radiation and Cloud Radiative Properties in the ECMWF Forecasting System', *J. Geophys. Res.* **96**, 9121–9132.

Pincus, R. and Baker, M. B.: 1994, 'Effect of Precipitation on the Albedo Susceptibility of Marine Boundary Layer Clouds', *Nature* **372**, 250–252.

Roeckner E., Arpe, K., Bengtsson, L., Brinkop, S., Dümenil, L., Esch, M., Kirk, E., Lunkeit, F., Ponater, M., Rockel, B., Sausen, R., Schlese, U., Schubert, S., and Windelband, M.: 1992, 'Simulation of the Present-Day Climate with the ECHAM-model: Impact of Model Physics and Resolution', Max-Planck Institute für Meteorologie, Report No. 93, Hamburg, 171 pp.

Roeckner H., Arpe, K., Bengtsson, L., Christoph, M., Claussen, M., Dümenil, L., Esch, M., Girogetta, M., Schlese, U., and Schulzweida, U.: 1996, 'The Atmospheric General Circulation Model ECHAM-4: Model Description and Simulation of Present-Day Climate', Max-Planck Institute für Meteorologie, Report No. 218, Hamburg, 90 pp.

Slingo, A. and Schrecker, H. M.: 1982, 'On the Shortwave Radiative Properties of Stratiform Water Clouds', *Quart. J. Roy. Meteorol. Soc.* **108**, 407–426.

Smith, R. N. B.: 1990, 'A Scheme for Predicting Layer Clouds and their Water Content in a General Circulation Model', *Quart. J. Roy. Meteorol. Soc.* **116**, 435–460.

Stevens, B.: 1996, *On the Dynamics of Precipitating Stratocumulus*, Ph.D. Dissertation, Colorado State University, Department of Atmospheric Science Paper 618, 140 pp.

Stevens, B., Cotton, W. R., Feingold, G., and Moeng, C.-H.: 1998, 'Large-Eddy Simulations of Strongly Precipitating, Shallow, Stratocumulus-Topped Boundary Layers', *J. Atmos. Sci.* **55**, 3616–3638.

Sundquist, H.: 1978, 'A Parameterization Scheme for Non-Convective Condensation Including Prediction of Cloud Water Content', *Quart. J. Roy. Meteorol. Soc.* **104**, 677–690.

Sundqvist, H., Berge, E., and Kristjansson, J. E.: 1989, 'Condensation and Cloud Parameterization Studies with a Mesoscale Numerical Weather Prediction Model', *Mon. Wea. Rev.* **117**, 1641–1657.

Tiedtke, M.: 1989, 'A Comprehensive Mass Flux Scheme for Cumulus Parameterization in Large-Scale Models', *Mon. Wea. Rev.* **117**, 1780–1800.

Tiedtke, M.: 1993, 'Representation of Clouds in Large-Scale Models', *Mon. Wea. Rev.* **121**, 3040–3061.

Tiedtke, M., Heckley, W. A., and Slingo, J.: 1988, 'Topical Forecasting at ECMWF: The Influence of Physical Parametrization of the Mean Structure of Forecasts and Analyses', *Quart. J. Roy. Meteorol. Soc.* 639–664.

Wyant, M. C., Bretherton, C. S., Rand, H. A., and Stevens, D. E.: 1997, 'Numerical Simulations and a Conceptual Model of the Subtropical Marine Stratocumulus to Trade Cumulus Transition', *J. Atmos. Sci.* **54**, 168–192.